Tau, Amyloid, and Cascading Network Failure across the Alzheimer's disease Spectrum

David T. Jones[1,2,*], **Jonathan Graff-Radford**[1], **Val J. Lowe**[2], **Heather J. Wiste**[3], **Jeffrey L. Gunter**[2,4], **Matthew L. Senjem**[2,4], **Hugo Botha**[1], **Kejal Kantarci**[2], **Bradley F. Boeve**[1], **David S. Knopman**[1], **Ronald C. Petersen**[1], and **Clifford R. Jack Jr.**[2]

[1]Department of Neurology, Mayo Clinic, Rochester, MN, USA.

[2]Department of Radiology, Mayo Clinic, Rochester, MN, USA.

[3]Department of Health Sciences Research, Mayo Clinic, Rochester, MN, USA.

[4]Department of Information Technology, Mayo Clinic, Rochester, MN, USA.

Abstract

Functionally related brain regions are selectively vulnerable to Alzheimer's disease pathophysiology. However, molecular markers of this pathophysiology (i.e., beta-amyloid and tau aggregates) have discrepant spatial and temporal patterns of progression within these selectively vulnerable brain regions. Existing reductionist pathophysiologic models cannot account for these large-scale spatiotemporal inconsistencies. Within the framework of the recently proposed cascading network failure model of Alzheimer's disease, however, these large-scale patterns are to be expected. This model postulates the following: 1) a tau-associated, circumscribed network disruption occurs in brain regions specific to a given phenotype in clinically normal individuals; 2) this disruption can trigger phenotype independent, stereotypic, and amyloid-associated compensatory brain network changes indexed by changes in the default mode network; 3) amyloid deposition marks a saturation of functional compensation and portends an acceleration of the inciting phenotype specific, and tau-associated, network failure. With the advent of *in vivo* molecular imaging of tau pathology, combined with amyloid and functional network imaging, it is now possible to investigate the relationship between functional brain networks, tau, and amyloid across the disease spectrum within these selectively vulnerable brain regions. In a large cohort (n = 218) spanning the Alzheimer's disease spectrum from young, amyloid negative, cognitively normal subjects to Alzheimer's disease dementia, we found several distinct spatial patterns of tau deposition, including 'Braak-like' and 'non-Braak-like', across functionally related brain regions. Rather than arising focally and spreading sequentially, elevated tau signal seems to occur system-

*Correspondence to: David T. Jones, Mayo Clinic, 200 First Street S.W., Rochester, MN 55905, jones.david@mayo.edu.

wide based on inferences made from multiple cross-sectional analyses we conducted looking at regional patterns of tau signal. Younger age-of-disease-onset was associated with 'non-Braak-like' patterns of tau, suggesting an association with atypical clinical phenotypes. As predicted by the cascading network failure model of Alzheimer's disease, we found that amyloid is a partial mediator of the relationship between functional network failure and tau deposition in functionally connected brain regions. This study implicates large-scale brain networks in the pathophysiology of tau deposition and offers support to models incorporating large-scale network physiology into disease models linking tau and amyloid, such as the cascading network failure model of Alzheimer's disease.

Keywords

Alzheimer's disease; cascading network failure; complex systems; AV-1451; Braak staging

1. Introduction

Alzheimer's disease is a progressive neurodegenerative disease that targets large-scale brain networks (Seeley *et al.,* 2009) leading to dementia over a timespan of decades. The cognitive domains supported by these networks, which decline as a function of targeted Alzheimer's disease pathophysiology, include memory, visual-spatial, sensorimotor, language, behavioral, and executive faculties (Petersen and Graff-Radford, 2016). The extent to which these cognitive functions are impaired in any individual varies greatly and is dependent on disease duration. The prototypical late-life onset phenotype, referred to as typical Alzheimer's disease dementia, begins with a memory-encoding deficit, before slowly involving other cognitive faculties in a heterogeneous fashion (Petersen, 2003). Atypical clinical variants begin with predominant non-memory clinical symptoms before involving other cognitive functions and commonly have a younger age of disease onset (Warren *et al.,* 2012).

The molecular hallmarks of this process include beta-amyloid (Aβ) plaques and neurofibrillary tangles (NFT), composed of the tau protein. The NFT burden is more closely associated with cognitive decline than Aβ plaques (Bennett *et al.,* 2004, Braak *et al.,* 1996, Dickson *et al.,* 1992, Duyckaerts *et al.,* 1997). Therefore, the pattern of tau protein deposition should resemble brain networks that support the cognitive functions that decline in Alzheimer's disease dementia (i.e., memory, visual-spatial, sensorimotor, language, behavioral, and executive systems) (Alladi *et al.,* 2007, Mesulam *et al.,* 2014, Murray *et al.,* 2011). Prior to this tau-associated cognitive decline, there is a long preclinical disease phase associated with Aβ plaques in the absence of significant tau pathology outside of the medial temporal lobe (Bateman *et al.,* 2012, Braak *et al.,* 1996, Dickson *et al.,* 1992). It remains unclear how these molecular hallmarks of Alzheimer's disease pathophysiology are mechanistically related across the spectrum of clinical and preclinical disease states. We have previously proposed a cascading network failure model of Alzheimer's disease pathophysiology, which incorporates systems-level pathophysiology into existing molecular disease models (Jones *et al.,* 2016). This model hypothesizes that synaptic remodeling/ burden, associated with compensatory shifts in large-scale network configurations, is related

to amyloidosis in hubs of high connectivity during the preclinical disease phase and tau pathology within specific networks during clinical disease stages. In other words, the model predicts that large-scale network changes would be related to both Aβ and tau. More specifically, it predicts that the relationship between network changes and tau would be partially mediated by pathophysiologic changes marked by Aβ deposition.

In this investigation, we evaluated these hypotheses by examining the relationship between biomarkers of network-wide pathophysiology and molecular pathophysiology. The model that is under investigation in this study is outlined in Figure 1. In the first part of our study, we used independent component analysis applied to [F-18]-AV-1451, a positron emission tomography ligand that was designed to detect Alzheimer's disease-related tau pathology (τ-PET) (Schwarz *et al.,* 2016, Xia *et al.,* 2013), to investigate distinct spatially independent patterns of tau deposition. This allowed us to isolate and quantify a typical, or 'Braak-like' (Braak *et al.,* 2006, Braak and Braak, 1991, Braak and Braak, 1997, Braak *et al.,* 2011), tau-deposition pattern that contains all of the brain regions needed for pathologic staging of NFT. In contrast to most autopsy studies, where tau deposition across the entire brain is not quantified in large numbers of subjects, we were able to investigate the emergence of this pattern across the entire brain and in doing so assess for cross-sectional evidence of system-wide tau deposition rather than sequential progression. In the second part of this study, we used data from τ-PET and Aβ-PET as measures of molecular changes and related this to functional network changes using task-free functional MRI (fMRI). The combined results of these analyses strongly implicate large-scale brain systems in the pathophysiology related to tau protein deposition and in the pathophysiology linking Aβ and tau, providing support for the model outlined in Figure 1.

2. Methods

2.1 Subjects

All participants were enrolled in either the Mayo Clinic Study of Aging or the Mayo Clinic Rochester Alzheimer's Disease Research Center. The Alzheimer's Disease Research Center is a longitudinal cohort study that enrolls subjects from the clinical practice at Mayo Clinic in Rochester, MN. The Mayo Clinic Study of Aging is a population-based study of cognitive aging among Olmsted County, MN residents (Roberts *et al.,* 2008). Enrolled participants are adjudicated to be clinically normal or have mild cognitive impairment by a consensus panel consisting of study coordinators, neuropsychologists and behavioral neurologists. Individuals who progress to dementia continue in the study. Methods for defining clinically normal, mild cognitive impairment and dementia in both of these studies conform to standards in the field (Albert *et al.,* 2011, McKhann *et al.,* 2011, Petersen, 2004). All clinically normal subjects who had high quality structural MRI, task-free fMRI, τ-PET, and Aβ-PET were included in this study. Subjects that were clinically impaired in the form of mild cognitive impairment (n = 11) or dementia (n = 30), were also included if they had these modalities available at the time of this study and their Aβ-PET standardized uptake value ratio (SUVR) exceeded 1.5, in order to increase the probability that Alzheimer's disease pathophysiology was contributing to their clinical impairment (Jack *et al.,* 2012). It should be noted that this higher threshold for Aβ-PET positivity was used to increase the

specificity for Alzheimer's disease pathophysiology in clinically impaired subjects, and no threshold was used in clinically normal subjects where a lower, more sensitive threshold is typically desired. See Table 1 for details regarding the cohort.

2.2 Standard protocol approvals, registrations, and patient consents

These studies were approved by the Mayo Clinic and Olmsted Medical Center Institutional Review Boards and written informed consent was obtained from all participants and/or their qualified representative.

2.3 Structural Magnetic Resonance Imaging

MRI was performed on one of three compatible 3T systems from the same vendor (General Electric, Waukesha, WI, USA). A 3D magnetization prepared rapid acquisition gradient echo (MPRAGE) structural imaging sequence developed for the Alzheimer's Disease Neuroimaging Initiative (ADNI) study was acquired (Jack *et al.,* 2008). All images were acquired using an 8-channel phased array head coil. Post-processing to correct for gradient distortion correction and processing has been validated in multiple studies, shown to give consistent stable results in ADNI data, and geometric fidelity after correction is independent of scanner (Gunter *et al.,* 2009, Vemuri *et al.,* 2015). Parameters were: TR/TE/T1, 2300/3/900 msec; flip angle 8 degrees, 26 cm field of view (FOV); 256×256 in-plane matrix with a phase FOV of .94, and slice thickness of 1.2 mm. These MPRAGE parameters have been held invariant since approximately 2008. This structural MRI was used for preprocessing PET and fMRI data. Spatially normalized and modulated gray matter intensities, derived from the SPM12 (http://www.fil.ion.ucl.ac.uk/spm/software/spm12/) unified segmentation and normalization algorithm, were also used to control for atrophy in some ROI and voxel-wise analyses described below.

2.4 PET Acquisition

The Aβ-PET imaging was performed with Pittsburgh Compound B (Klunk *et al.,* 2004) and τ-PET with AV-1451 (Schwarz *et al.,* 2016, Xia *et al.,* 2013). PET images were acquired using 1 of 2 PET/CT scanners (DRX; GE Healthcare) operating in 3-dimensional mode (septa removed). A computed tomography scan was obtained for attenuation correction. Aβ-PET images were acquired from 40–60 minutes after injection of 628 MBq (range 385 to 723 MBq) and τ-PET from 80–100 minutes after injection of 370 MBq (range 333–407). PET sinograms were iteratively reconstructed into a 256 mm FOV. The pixel size was 1.0 mm and the slice thickness 3.3 mm. Standard corrections were applied.

2.5 Aβ-PET Analysis

Amyloid PET images were analyzed with our in-house, fully automated image processing pipeline (Senjem *et al.,* 2005) wherein image voxel values are extracted from automatically labeled regions of interest (ROIs) propagated from an MRI template. A global Aβ-PET SUVR was calculated as the median uptake in the prefrontal, orbitofrontal, parietal, temporal, anterior and posterior cingulate and precuneus ROIs normalized to the cerebellar gray median. However, voxels whose probability of being CSF was greater than the

probability of being grey matter or white matter, based on co-registered segmented MRI, were not included in the calculation.

2.6 Spatial Patterns of τ-PET Deposition: Independent Component Analysis

In order to identify and quantify unique spatial patterns of tau deposition across the entire cohort we used spatial independent component analyses (ICA), a blind source separation technique, to explore the τ-PET data in an unbiased and model free fashion. Each subjects' τ-PET scan was spatially normalized to the Mayo Clinic Study of Aging template space (https://www.nitrc.org/projects/mcalt) using the structural image based unified segmentation and normalization procedure in SPM12, intensity normalized using the cerebellar crus gray matter as reference, and smoothed with an 8 mm full-width half maximum Gaussian kernel. These images were then entered into a spatial ICA using the infomax method implemented in Group ICA Toolbox (http://mialab.mrn.org/software/#gica), with the dimensionality of 33 being determined using minimum description length (MDL) criterion. Rerunning the ICA procedure with bootstrap sampling repeated 100 times revealed highly-stable components. We also repeated this analysis at a higher dimensionality (i.e. 70). The high-dimensional ICA produced less stable components, but our main component of interest (discussed in detail in the results section) was nearly identical at the higher-dimensional ICA level (data not shown). Therefore we report the results of the ICA analysis performed at the dimensionality determined by the MDL criteria (i.e., 33). The preprocessed τ-PET scans for all subjects (n = 218) were included in the ICA to identify group-level, voxel-wise, spatially independent patterns of τ-PET signal and subject-level *loadings,* or *subject component scores,* for each pattern. Five of the 33 independent components (ICs) were related to the relevant Alzheimer's disease neurobiology in that they showed a strong Aβ-PET relationship (i.e., significantly higher component scores in subjects with Aβ-PET SUVR > 1.5 than subjects with SUVR < 1.5, Bonferroni corrected P < 0.001). The remaining components were related to non-specific signal or brain structure (e.g., ventricles, white matter, etc.). Key regions of off-target binding (Lowe *et al.,* 2016), which typically confound ROI-based assessment, separated into distinct ICs with no association to Aβ-PET. For example, signal in the choroid plexus IC was not related to Aβ-PET or cortical thickness (P = 0.13) but was related to advancing age (β = 0.21, P = 0.002) (see Supplementary Figure 1). This is in contrast to the five ICs related to Alzheimer's disease pathophysiology described in the results section.

We created 5 IC based ROIs by binarizing each IC with a hard threshold of a z-score of 5. In order to evaluate the correspondence between ROI tau-PET SUVR and subject component scores we used a multiple regression model associating subject component scores with τ-PET SUVR while controlling for gray matter density in these same ROIs. A similar analysis was performed at the voxel-level.

2.7 Spatial Patterns of τ-PET Deposition: Voxel-Wise Frequency

All of the Braak NFT regions necessary for staging AD under the Braak NFT schema were in the same spatial independent component (Supplementary Figure N2). This was true for both the low-dimensional and high-dimensional ICA. The lack of spatial independence between τ-PET signal in these brain regions implies that they would therefore have the same

frequency of involvement in AD. This was surprising and inconsistent with what is found pathologically, where the entorhinal cortex is more frequently found to have tau pathology relative to other brain regions. Therefore, we next attempted to visualize how frequently brain regions had abnormally elevated signal across this cohort on a voxel-level. We created a frequency map of voxels with high tau levels defined as greater than 3 standard deviations above the uptake in cognitively normal, Aβ-negative individuals with the least evidence of these tau patterns being present (i.e., the 50 subjects with most negative subject component scores).

We also report the results from these voxel-wise frequency maps using predefined "Braak ROIs" in order to report results using Braak regions. The Braak ROIs were constructed as previously described (Scholl *et al.,* 2016). We then calculated the voxel-wise frequency of elevated τ-PET signal per Braak ROI and report the peak frequencies with the Braak ROIs at three thresholds for defining elevated PET signal ($z = 1$, $z = 2$, and $z = 3$).

2.8 Spatial Patterns of τ-PET Deposition: Mixed-Effects Modeling of the Relationship between τ-PET and Aβ-PET by Brain Region

In order to investigate the regional variation in τ-PET signal free from any potential bias related to arbitrary thresholds present in the voxel-wise frequency analyses, we extracted the τ-PET signal from the three brain regions identified as most frequently having abnormally elevated levels of tau (i.e., entorhinal, inferior temporal, and dorsal precuneus) and modeled those values against global Aβ-PET. Regions with a higher frequency of abnormal τ-PET signal might be expected to show signal elevation sooner (i.e., at lower Aβ-PET SUVR levels) than lower frequency brain regions, which would manifest as a steeper slope in the cross-sectional analyses of τ-PET vs. Aβ-PET. Therefore, we used linear mixed-effects modeling with random slopes and intercepts for subjects to investigate the effect of brain region (i.e., entorhinal, inferior temporal, and dorsal precuneus) on the relationship between τ-PET and Aβ-PET.

2.9 Spatial Patterns of τ-PET Deposition: Average τ-PET Maps Across the Disease Spectrum

To further investigate the emergence of the typical spatial pattern of τ-PET signal across the Alzheimer's disease spectrum, we divided the subjects into groups using breaks along subject component scores for the typical τ-PET pattern and created voxel-wise group average τ-PET maps. The breaks were defined in order to capture various portions of the sigmoidal relationship between τ-PET and Aβ-PET. All of the subjects with negative loadings, occupying the initial slowly rising phase of the sigmoid, were placed into a single group. The initial emergence of the pattern (i.e., IC-5 subject scores > 0) was divided into more fine grained groups, capturing the earliest changes in the τ-PET pattern and allowing for more frequent sampling along various points of the sigmoidal relationship between Aβ and the typical τ-PET pattern. The plateau portion of the sigmoid was combined into one group. These breakpoints are highlighted in Supplementary Figure 3. Patient characteristic (e.g. age, clinical status, Aβ-PET SUVR, τ-PET SUVR, and fMRI) were also compared across these groupings.

2.10 Task-Free fMRI Preprocessing and Network Measures

Task-free fMRI data were acquired using an 8 channel head coil, gradient echo planar imaging, TR = 3000 ms, TE = 30 ms, 90° flip angle, 21 cm field of view, 64×64 in-plane matrix, slice thickness 3.3 mm without gap, and 103 volumes were obtained. Subjects were instructed to keep their eyes open during scanning. All task-free fMRI data sets with greater than 3 mm of translational movement, 3° of rotational movement, or that failed visual inspection for obvious artifacts were excluded from analysis.

The methods recently developed for analyzing task-free fMRI data in the Alzheimer's disease Neuroimaging Initiative were adapted for the task-free fMRI portion of this study. After preprocessing, as previously described (Jones *et al.,* 2016), a spatial–temporal regression was performed within a multivariate framework incorporating all four default mode network (DMN) subsystems of interest using functions from the GICA of functional MRI Toolbox (GIFT v2.0e) software package (Calhoun *et al.,* 2001). The four DMN subsystem measures that we had previously shown to change linearly (both increases and decreases) in the ADNI cohort across the disease spectrum, as part of the cascading network failure (i.e., the posterior DMN, ventral DMN, posterior-to-ventral DMN, and posterior-to-anterior dorsal DMN connectivity), were used to create a recently described (Wiepert *et al.,* 2017) single summary metric of network failure termed the Network Failure Quotient (NFQ).

$$\mathrm{NFQ} = \frac{\mathrm{pDMN\_ to\_ vDMN} + \mathrm{pDMN\_ to\_ adDMN}}{\mathrm{pDMN} + \mathrm{vDMN}}$$

This summary biomarker of the cascading network failure was used in a mediation analyses to test our model predictions (Figure 1) regarding the relationship between tau, networks, and amyloid. With the results of the mediation analysis in hand, we performed nested post-hoc voxel-wise analyses to more fully explore that nature of the association between tau, large scale brain network changes, and amyloid. First, in order to see if there was any difference in the local tau deposition patterns associated independently with global Aβ and NFQ, we created spatial maps of the t-scores of the Aβ and NFQ terms in a linear model predicting τ-PET signal on a voxel level while controlling for age. The independent patterns associated with Aβ and NFQ were qualitatively similar to two of the patterns captured by the spatial ICA (IC-5 and IC-4, respectively). Next, we conducted another exploratory analysis to determine if there were two distinct posterior DMN functional connectivity patterns associated with the tau pattern captured by IC-5 and IC-4, as our model would predict. This was done by creating spatial maps of the t-scores of the IC-5 and IC-4 terms in a linear model predicting posterior DMN functional connectivity on a voxel level while controlling for age.

2.11 Statistical Procedures

A combination of MATLAB-based (Mathworks Inc., Natick, MA, USA) and R-based (http://www.R-project.org) software packages were used to perform all statistical analysis. We used linear mixed-effects modeling with random slopes and intercept for subjects to investigate the effect of brain region (i.e. entorhinal, inferior temporal, and dorsal precuneus)

on the relationship between τ-PET and Aβ-PET using functions from the R–package lme4 (Bates *et al.,* 2015). We investigated non-linearity between τ-PET and Aβ-PET within general additive models using penalized regression splines (Wood, 2006). The R-package 'mediation' was used to perform the mediation analysis (Tingley *et al.,* 2014). A bootstrapping procedure was used to derive 95% CIs for each of these models where indicated. Kruskal-Wallis one-way ANOVA was used for continuous variables, with post-hoc Mann-Whitney U-tests for pair-wise differences. Chi-squared tests were used for categorical variables.

3. Results

3.1 Tau-PET covaries spatially within several distinct brain systems and is associated with age of disease onset

Each of the five τ-PET IC patterns which were associated with Aβ-PET status involved brain regions that are functionally related (Figure 2). All of these ICs will be made available via individual requests sent to the corresponding author and the peak coordinates are summarized in Supplementary Table 1. The visual network pattern captured in IC-1 symmetrically involved visual association cortices and had spatial overlap (Dice coefficient of similarity = 0.64) with the ventral visual stream resting state network in the Mayo Clinic Study of Aging Functional Connectivity Atlas (Jones et al., 2012). The visual/executive pattern captured in IC-2 spanned right lateralized brain regions across visual association, parietal, and frontal brain regions and did not overlap with a particular resting state network from our atlas to produce a Dice coefficient greater then 0.20, but did overlap with portions of several visual and executive networks. The pattern captured in IC-3 involved left lateralized fronto-parietal brain regions that strikingly mirror the left working-memory resting state network (Dice coefficient of similarity = 0.49, see Supplementary Figure 4). The pattern captured in IC-4 mainly involved the precuneus and overlapped with the posterior DMN from our atlas (Dice coefficient of similarity = 0.57). The pattern captured in IC-5 did not follow a single resting state network, but did closely follow regions sampled in the Braak NFT pathologic-staging schema (Supplementary Figure 2). Given the intense involvement of the temporal lobe in IC-5, in addition to selected extra-temporal regions, no network showed a strong resemblance to this component. However, the extra-temporal portions of IC-5 do closely follow all of the key regions of the ventral DMN (data not presented). This is an interesting observation that may relate to the selective involvement of the ventral DMN in typical clinical presentation of AD dementia in contrast to atypical presentations (Whitwell *et al.,* 2015), but this will require a dedicated analysis beyond the scope of the current investigation.

We observed that the regions captured by IC-5 included all of the regions that are commonly sampled in pathologic studies of Braak NFT staging (see Supplemental Figure 2). We found this to be a striking data driven way of defining these regions, with the weighting (i.e., subject component score) of the IC-5 component simultaneously scoring all of the routinely sampled brain regions for Braak-staging (Alafuzoff *et al.,* 2008). Not only were all of these regions simultaneously included in IC-5, but the gradient evident in the spatial map of IC-5 also followed the expected Braak-gradient in terms of hypothesized temporal sequence of

involvement of brain regions (i.e., an implied temporal sequence of tau in cross-sectionally sampled regional magnitude, or frequency of involvement, with lower Braak stage regions like the entorhinal cortex exceeding higher Braak stage regions like the visual cortex). This gradient is clearly evident in the voxel-wise maps, and particularly evident when adjusting for biological signal-to-noise (SNR) which is described in more detail below in the section 3.2 (*Elevated τ-PET signal distributed similarly across Braak NFT Regions*). Further, we quantitatively verified that the expected Braak-gradient was indeed present by using pre-defined "Braak ROIs" as previously described (Scholl *et al.*, 2016). These Braak ROIs collapse the Braak NFT stages into three regions with the expected Braak-gradient being BR I/II > BR III/IV > BR V/VI. We calculated the median z-score in each Braak ROI for each of the 5 spatial ICA maps. We found that only IC-5 followed the expected Braak-gradient and that this was most evident after adjusting by biological SNR (Supplementary Figure 5). We therefore refer to IC-5 as the typical, or 'Braak-like,' tau pattern because all off the brain regions needed for Braak staging were included in one component and the Braak-gradient is evident in the weighting of that spatial pattern, allowing for a Braak-like stage to be summarized in one number (i.e. the subject component score for IC-5) rather than using three separate numbers for each Braak ROI. This observation may explain why Braak ROIs do not outperform global measures of τ-PET (Maass *et al.*, 2017). The other components do not meet these criteria and are referred to as atypical, or 'non-Braak-like' patterns. This designation was also supported by our analyses of subject component scores versus age of disease onset (see next paragraph). This is because atypical clinical (Warren *et al.*, 2012) and pathologic phenotypes (Murray *et al.*, 2011) are associated with younger-age of disease onset.

We investigated the association of each of these τ-PET patterns with age of disease onset in 32 of the impaired subjects for whom this information was known (Figure 2 inset plots). The four atypical tau deposition patterns were more common in subjects with a younger age of onset, but this relationship was only significant for IC-3 ($P < 0.01$) and IC-2 ($P = 0.01$). The Braak-like pattern of tau deposition was not associated with age of disease onset ($P = 0.39$).

The five ROIs used to extract τ-PET SUVR values to compare to subject component scores are displayed in Figure 3. Given the nature of the spatial ICA, there is little spatial overlap in the ROIs; however areas of overlap are highlighted in Figure 3. The average τ-PET SUVR magnitude from these ROIs was strongly associated with each of the subject component scores (correlations ranging from 0.81 – 0.91) confirming that the ICs are capturing the τ-PET signal of interest, as the ICs of non-interest are not correlated with τ-PET SUVR. A Braak-like τ-PET pattern subject component score of zero corresponds to a τ-PET SUVR of ~1.36 in those brain regions. Given that we recently reported a conservative τ-PET SUVR cut point of 1.33 (Jack *et al.*, 2017), in the current study we consider a positive (greater than zero) subject component score as indicating elevated tau-PET signal. These correlations persist even after controlling for gray matter density and are linear through the entire cohort free from outlier bias (Supplementary Figure 6). In a post-hoc voxel-wise analyses controlling for gray matter density at each voxel, these subject component scores were strongly predictive of τ-PET SUVR in a spatially unique way for each IC (Supplementary Figure 7). These analyses support the conclusion that the originally identified ICs capture 5 distinct spatial patterns of elevated tau deposition. We also compared our ICA approach to a

more traditional reporter ROI SUVR method by correlating the subject component scores for each ROI with the SUVR from an entorhinal cortex ROI. We find a high correlation between our ICA approach and the SUVR based reporter ROI approach with correlations ranging from 0.56 to 0.79. The typical Braak-like pattern (IC-5) had the strongest correlation with the entorhinal cortex reporter ROI, which also supports using IC-5 as the representative τ-PET subject component score. The advantage of using the ICA based method, rather than the reporter ROI SUVR value, is that the ICA method is data driven and incorporates biologically relevant information in the PET images outside the reporter ROI and is not contaminated by atrophy effects or off target binding that separates out into separate independent components of τ-PET signal. The ICA approach also allows for separating out distinct patterns of tau deposition rather than forcing all potential patterns into a signal *a priori* defined ROI-based schema.

There was a large amount of between-subject heterogeneity in the expression of these 5 τ-PET patterns (Supplementary Figures 8–12), including subjects with typical Alzheimer's disease dementia. Intriguingly, a posterior cortical atrophy subject showed relatively greater loadings in IC-1 and 2 (visual and visual/executive respectively) compared to the typical Braak-like pattern (IC-5). Additionally, one subject with a corticobasal syndrome phenotype and autopsy proven pathologic AD, showed negative loadings in the typical Braak-like pattern and high loadings on every other component despite there being τ-PET signal in the temporal lobe (Supplementary Figure 9). Subjects with amnestic mild cognitive impairment (n = 8) all had positive loadings for the typical Braak-like pattern (IC-5) which is in contrast to non-amnestic (n = 3) and dementia with Lewy bodies subjects (n = 3) who had negative or near zero loadings on IC-5 (Supplementary Figure 10). Marginally elevated levels of the Braak-like and non-Braak-like patterns were present in a subset of both amyloid positive (dark gray plots in Supplementary Figure 11) and amyloid negative subjects (light gray plots in Supplementary Figure 11, and see Supplementary Figure 12 for a case example).

3.2 Elevated τ-PET signal distributed similarly across Braak NFT regions

The frequency map of voxels with high tau levels largely recapitulated the typical tau pattern (Figure 4). Surprisingly, however, the tau deposition frequency in the dorsal precuneus and posterior inferior temporal lobe was nearly the same as the frequency in entorhinal regions. The spatial pattern of the result was not altered by lowering the threshold for determining a positive voxel or by changing the group used to define the z-score. While this phenomenon is apparent in the voxel-wise map presented in Figure 4, we also verified this fact using predefined Braak ROIs (Scholl *et al.,* 2016). We determined the most frequently abnormal voxel at three thresholds (z-score of 1, 2, or 3) within each Braak ROI and plotted that as the percentage of subjects that had a τ-PET scan with elevated signal in that voxel. This analysis was in agreement with the voxel-wise analysis presented in Figure 4 in that no Braak-gradient was evident at any threshold (Supplementary Figure 13).

In order to investigate the τ-PET signal in these regions free from any potential bias related to arbitrary threshold levels, the group chosen to anchor the threshold, or assumptions made in the independent component analysis, we extracted the τ-PET signal from these three brain regions and plotted those against Aβ-PET (Figure 5). We found that there was a significant

effect of brain region on the relationship between τ-PET and Aβ-PET (t = 4.41, p < 0.001), with post-hoc pair-wise comparison being significant for all pairs of brain regions. However, the pattern was unexpected in that the slope was greatest in the inferior temporal regions and lowest in the entorhinal region (Figure 5A).

Inspection of the plot reveals that this result is biased by the biological signal-to-noise (SNR) across the Alzheimer's disease spectrum. For example, the entorhinal region did not have the same magnitude of τ-PET signal change in Alzheimer's disease dementia subjects as other regions, and this lead to the observed difference in slope. However, the entorhinal cortex did have markedly reduced variability compared to other brain regions. Once the values in each of the three brain regions were standardized by the average magnitude and variance across the disease spectrum, another pattern emerged (Figure 5B). The significant effect of brain region on the relationship between τ-PET and Aβ-PET (t = −5.64, p < 0.001) remains, but without any difference between the inferior temporal and entorhinal regions (t = 1.57, p = 0.12). The fact that signal differences between the entorhinal and inferior temporal regions disappeared after standardization is compatible with the fact that they were included in the same independent component with a greater weighting in inferior temporal regions (Figure 2E, and Supplementary Figure 14A). In other words, our threshold-free ROI-based analyses are well in line with our frequency plot and our original ICA analysis in which all Braak-regions remained in the same IC. Intriguingly, once we adjusted the 'Braak-like' IC pattern (Supplementary Figure 14A) by the voxel-wise biological SNR (Supplementary Figure 14B), the Braak NFT pathologic-staging schema was very closely approximated (Supplementary Figure 14C). The biological SNR adjusted IC-5 map also had the most evident Braak-gradient (Supplementary Figure 5F). This demonstrates that τ-PET signal does indeed measure all regions in the Braak NFT schema in a manner that would be predicted by the pathologic literature, but statistical properties and off target signal contamination need to be accounted for in order to observe these changes. A recent ROI-based analysis (Johnson *et al.,* 2016) was not able to demonstrate significant hippocampal signal change given that this approach has more difficulty in dealing with regional variation in disease-related tau-signal increases and contamination with 'off target' binding in adjacent structures.

The voxel-wise average τ-PET maps created across the AD spectrum suggest a similar system-wide increase in τ-PET signal, rather than a sequential spread (Figure 6). There was little evidence of elevated average τ-PET signal in subjects with negative loadings (IC score < 0), but component scores in these subjects still displayed age-associated increases (β = 0.58, P < 0.001) consistent with recent reports (Scholl *et al.,* 2016) and with existing pathologic literature (Crary *et al.,* 2014). Elevated average levels of tau-PET become visually apparent in subjects with positive loadings, and signal was present simultaneously throughout the regions identified by the typical τ-PET pattern. However, between IC score levels of 0.5 – 1.0, there was a large increase in the magnitude of the signal throughout the system. Around this same point, there was a significant increase in the proportion of Aβ positive subjects (bottom half of Figure 6), and there was a greater degree of network failure present as measured by NFQ. The other molecular, clinical, and network measures are compared and presented for each IC group in the inset of Figure 6. A video combining

Figures 6 and Supplementary Figure 3 is available as a supplement (Supplementary Video 1).

3.3 Beta amyloid partially mediates the relationship between functional network failure and tau deposition

In order to more directly investigate how these network-based patterns of tau deposition relate to measures of functional connectivity in large-scale brain networks, we studied the relationship between τ-PET and a task-free fMRI based biomarker of network failure (i.e., the NFQ). All three measures were associated with age across the disease spectrum and in clinical normal subjects; therefore all models include age as a covariate. Importantly, we recently reported that among clinically normal subjects, τ-PET is not associated with NFQ when age is included in a multivariate model suggesting that age-related factors other than entorhinal cortex tau can drive NFQ prior to amyloid accumulation and cognitive impairment (Wiepert *et al.,* 2017).

Network failure was associated both with Aβ-PET ($\beta = 0.34$, $P < 0.001$) and the typical tau pattern ($\beta = 0.31$, $P < 0.001$ and see group comparison in Figure 6). Therefore, we performed a mediation analysis to test whether the relationship between network failure and tau was mediated fully, partially, or at all by Aβ. As an important prerequisite to performing the mediation analysis, we had previously observed the association between Aβ-PET and the typical tau pattern. The mediation analysis was consistent with one third of the relationship between network failure and tau being direct (direct effect 0.26, 95% CI [0.02, 0.46]) and the remaining 67% (95% CI [45%, 97%]) being mediated by amyloid (mediation effect 0.52, 95% CI [0.30, 0.79] with a total effect of 0.78, 95% CI [0.45, 1.11]) (Figure 7A). Given the potential circularity confound regarding IC selection and amyloid, we repeated this mediation analysis substituting the reporter ROI SUVR-based approach for IC-5 component scores and found the same results. In order to see if there was any difference in the local tau deposition pattern associated independently with global Aβ and NFQ, we created spatial maps of the t-scores of the Aβ and NFQ terms in a linear model predicting τ-PET signal on a voxel level while controlling for age (equation in Figure 7A). This demonstrated that global Aβ was relatively more associated with medial and lateral temporal tau deposition than the precuneus in a pattern recapitulating IC-5 (Figure 7B). This was in contrast to the pattern observed for NFQ, which had a relatively greater association with tau in the precuneus compared to the medial and lateral temporal regions in a pattern recapitulating IC-4 (Figure 7C). These results are in line with a recent regional analysis of tau, amyloid, and gray matter (Sepulcre *et al.,* 2016).

3.4 Posterior DMN connectivity patterns associated with tau-PET are distinct for tau in the temporal lobe versus the precuneus

This result then lead to our analyses of IC-5 and IC-4 as a predictor for posterior DMN connectivity (see the equation at the bottom of Figure 7). This was in-line with the model presented in Figure 1. IC-5 was associated with hyper-connectivity within the posterior DMN (e.g., the precuneus) and increased connectivity to a variety of other brain regions as would be predicted in step 2 outlined in Figure 1 (Figure 7D). IC-4, or the precuneus/posterior DMN specific tau deposition, was associated with declining posterior DMN

connectivity in the precuneus and increased frontal lobe connectivity (Figure 7E). This explains why the NFQ is associated with the IC-4 pattern of tau deposition, and is consistent with step 3 outlined in Figure 1. However, none of the results in Figure 7 D and E survived correction for multiple comparisons and should be considered post-hoc and exploratory, but well-grounded in the results leading to this analyses.

4 Discussion

Our major findings were: (1) Spatial patterns of tau deposition follow functionally related brain systems, beyond those sampled neuropathologically for Braak staging, in a heterogeneous manner; (2) These atypical, 'non-Braak-like' tau-deposition patterns were associated with younger age-of-onset while the typical, 'Braak-like' pattern was not related to age-of-onset; (3) Elevated τ-PET signal is detected network-wide rather than focally and sequentially throughout Braak regions as demonstrated by ICA (Figure 2E and Supplementary Figures 2,5, and 14), frequency count (Figure 4 and Supplementary Figure 13), the effect of brain region on the relationship between tau and Aβ (Figure 5), average τ-PET images across IC-5 loading groups (Figure 6), and the presence of network wide patterns in clinically normal subjects (Supplementary Figures 11 and 12 and recently reported in (Mishra *et al.,* 2017)); (4) The typical, 'Braak-like' τ-PET deposition pattern is related to large-scale functional network failure, with this relationship being partially mediated by Aβ (Figure 7). These results implicate large-scale brain networks in the pathophysiology of tau and in the pathophysiology that links Aβ to tau as hypothesized by our model outlined in Figure 1.

The cascading network failure model is consistent with these cross-sectional observations, but it is not the only potential interpretation (see more detailed discussion below). This is certainly true regarding hypotheses relating to temporal sequences of events. Longitudinal analyses across the AD-spectrum will be required to truly examine temporal predictions made by our model and alternative models. All prior studies of the temporal progression of tau have been forced to make inferences from cross-sectional pathologic data, but with the advent of τ-PET, true longitudinal studies are now possible. However, reports of cross-sectional observations necessarily precede detailed longitudinal studies and these observations can be interpreted in light of prior cross-sectional pathologic studies.

4.1 Elevated levels of τ-PET signal appear across large-scale brain networks

This study demonstrates that the spatial patterns of tau deposition can follow functionally related brain regions beyond those usually sampled neuropathologically for Braak staging (Figure 2), which has been the focus of several τ-PET investigations (Cho *et al.,* 2016, Johnson *et al.,* 2016, Scholl *et al.,* 2016, Schwarz *et al.,* 2016). This is consistent with recent reports of differences in τ-PET uptake between specific clinical phenotypic variants of Alzheimer's disease (Ossenkoppele *et al.,* 2016). Further support for the notion that τ-PET patterns more closely capture network-related variability, which manifests as different clinical phenotypes, comes from the striking correspondence of τ-PET patterns and three resting state networks (ventral visual stream, posterior DMN, and the left working memory network [Supplementary Figure 4]). In further support of this association with phenotypic

heterogeneity, the left working-memory network is a system thought to underlie the phonologic loop (Baddeley and Hitch, 1974), which we have recently shown to be more affected in language presentations of Alzheimer's disease (Whitwell *et al.,* 2015). However, as is apparent to clinicians and caregivers, there remains a large amount phenotypic heterogeneity even in so-called 'typical' presentations of Alzheimer's disease (Supplementary Figure 8). As such, the different patterns of tau deposition identified in our study are relevant to studies of all phenotypic presentations of Alzheimer's disease, as well as all clinical stages, extending across preclinical, mild cognitive impairment, and dementia (Supplementary Figures 8–12). In fact, isolating the extent to which these tau deposition patterns are present has great potential to serve as a new phenotypic tool that may be more precise than recapitulating the Braak staging schema using Braak ROIs (Scholl *et al.,* 2016). Cognitive domain and phenotype-specific correlations with τ-PET patterns were not the focus of this current study, but future studies into these associations are needed.

It was surprising that Braak NFT staging regions were all present within the same τ-PET IC pattern (Figure 2E and Supplementary Figures 2,5, and 14). This is an unexpected result because early Braak regions, such as the entorhinal cortex, should have elevated tau-PET signal that occurs independently and with greater frequency than later Braak regions (e.g. the inferior temporal cortex) and therefore result in an independent component that is composed only of early Braak regions. However, this did not occur in either the low-dimensional (i.e., 33) or the high dimensional (i.e. 70) spatial ICA analysis. This result raises the possibility that τ-PET signal in Braak NFT regions may not be independent - although, the cross-sectional ICA analysis may be biased. Our result from mapping elevated τ-PET signal by the frequency of involvement of each brain voxel also indicates that several regions across the brain have detectable increased tau-PET signal simultaneously (Figure 4). This can also be observed in clinically normal subjects without evidence of elevated Aβ (Supplementary Figure 11 and 12). In addition to the entorhinal regions, the posterior inferior temporal cortex and dorsal precuneus were abnormal in a large proportion of subjects (Figure 4 and Supplementary Figure 13). While this may not necessarily indicate that the signal simultaneously becomes abnormal in all of these regions, it does argue against a sequential involvement of Braak regions with limbic structures becoming involved before neocortical regions, as one would expect from a seed-based templating mechanism following the Braak staging gradient. Sequential spreading not fully detected by τ-PET until later stages could also produce these observations, but using Braak-staging ROIs, or any other regional approach, would not confer any particular advantage over global measures in such a case (Maass *et al.,* 2017). The lack of utility in using Braak-staging ROIs is also highlighted by the fact that the τ-PET signal in preclinical AD is more widespread than predicted by pathologic staging as was recently shown by others (Mishra *et al.,* 2017) and also observed in this study (see Figure 6 and Supplementary Figures 11–13). Another alternative explanation for the observed widespread signal is that tau-PET is sensitive to abnormalities in vulnerable brain systems even in the absence of NFTs, perhaps manifesting as marginally elevated tau-PET signal. All three of these possibilities would appear as synchronously elevated τ-PET signal rather than recapitulating the sequential involvement that has been inferred from cross-sectional pathologic studies.

It is uncertain if there is a neuropathological correlate for the τ-PET signal in these brain regions at early Braak NFT stages, as they are not all routinely sampled as part of the Braak NFT-staging schema and the probability of observing tau in these regions likely varies. It appears that the major difference between these brain regions is the biological SNR (Figures 5 and Supplementary Figure 14) rather than the frequency of involvement *per se* (Figure 4 and Supplemental Figure 13). The fact the differences between these regions is largely related to SNR is also consistent with statistical differences observed between these brain regions and their correlation with clinical variables (Maass *et al.,* 2017). Even when we separated out subjects by typical Braak-pattern loadings (Figure 6 and Supplementary Video S1), we did not appreciate a pattern of sequential involvement in these brain regions, but more of a 'blooming' of the τ-PET signal throughout Braak regions with progressive increase in the intensity of the signal. We also observed the presence of these IC patterns (indicating signal throughout the system) in clinical normal subjects without elevated Aβ levels (Supplementary Figures 11 and 12). Longitudinal τ-PET studies spanning the Alzheimer's disease spectrum will be needed to investigate this apparent emergence of τ-PET signal diffusely within functional systems.

4.2 The relationship between Aβ-PET and τ-PET

The majority of the variability in τ-PET can be explained by Aβ-PET, with similar percentages found using generalized additive models (Supplementary Figure 2, 65.8% of the deviance, $p < 0.001$) and in the mediation analyses with network failure (67%, 95% CI [45%, 97%]). However, the relationship is non-linear and appears more sigmoidal (Supplementary Figure 3), consistent with proposed biomarker models (Jack *et al.,* 2013, Villemagne *et al.,* 2013). The change in Aβ-PET plateaus, as has been reported previously (Jack *et al.,* 2013); however, τ-PET continues to increase as the proportion of clinically impaired subjects increases (Figure 6), suggesting that τ-PET is a better marker of progression in the clinical disease phase (Brier *et al.,* 2016), while Aβ-PET is a better marker of preclinical disease stages. Given that τ-PET appears to continue to increase after amyloid saturation, this may drive the partial independent association between NFQ and tau from Aβ (Figure 7). In this context, it is interesting to note that the global Aβ is more associated with the spatial pattern captured in IC-5 (typical Braak pattern, Figure 7B) and NFQ is more associated with the pattern captured by IC-4, which resembles the posterior DMN (Dice coefficient of similarity = 0.57) centered in the precuneus (Figure 7C). In addition, the posterior DMN connectivity patterns associated with tau-PET are distinct for tau in the temporal lobe (Figure 7D) versus the precuneus (Figure 7E). This pattern and the apparent temporal sequence are largely in keeping with the cascading network failure model discussed in more detail below and outlined in Figure 1.

It is still unclear why there is an apparent temporal lag between markers of Aβ increase and markers of tau increase. In addition, Aβ deposition occurs throughout all major hubs of connectivity in the brain (Buckner *et al.,* 2009), while tau deposition occurs within specific functional networks (Figure 2) and not in major hubs in general. Existing models have struggled to account for these spatiotemporal gaps between the two major molecular hallmarks of the disease. Invoking pathophysiologic mechanisms that incorporate large-scale

brain systems may shed light on this long-standing apparent spatiotemporal paradox between Aβ and tau (Jones *et al.,* 2016, Stam, 2014).

4.3 Large-scale brain networks and protein deposits

There are many open questions regarding the mechanistic link between large-scale brain networks and neurodegenerative diseases, despite the long-known fact that connected systems are important aspects of neurodegenerative pathophysiology. Over the years, several monikers have been proposed to capture this relationship, such as systems degenerations (Saper *et al.,* 1987), network-based neurodegeneration (Greicius and Kimmel, 2012), and molecular nexopathies (Warren *et al.,* 2013). Seed-based polymerization of various proteins spreading along structural brain connections is currently the most widely accepted hypothesis for the observed associations between neurodegenerative patterns and network properties (Raj *et al.,* 2012, Zhou *et al.,* 2012). However, questions remain regarding the explanatory ability of these models (Walsh and Selkoe, 2016), and they have not accounted for the spatiotemporal gap between the two major molecular hallmarks of Alzheimer's disease. In fact, recent tests of the seed-based polymerization model failed to achieve as strong of evidence for Alzheimer's disease as for other neurodegenerative diseases studied (Zhou *et al.,* 2012). The authors speculate that it may be the dual-protein nature of Alzheimer's disease that led to this discrepancy. Therefore, while seed-based polymerization may explain portions of tau pathophysiology in Alzheimer's disease, it does not explain Aβ pathophysiology or the stereotypical spatiotemporal gaps between tau and Aβ. In addition, τ-PET signal seems to be detectable in multiple brain regions across functional networks simultaneously rather than in a step-wise manner, which is more supportive of selectively vulnerable brain systems being the etiology as opposed to seed-based templating, although, both mechanisms may occur simultaneously (Walsh and Selkoe, 2016). In this context, it should be noted that functionally connected brain systems, centered in the parietal and posterior cingulate regions, have been found to be abnormal in mouse models of age-related memory impairment, and that this functional stress is alleviated with therapies targeting brain circuits (Haberman *et al.,* 2017).

The cascading network failure model may be better able to account for these discrepancies by reconciling distributed network level pathophysiology with proposed molecular pathophysiological mechanisms (Figure 1). It is clear that synaptic activity and plasticity are related to the (patho)physiology of Aβ (Palop and Mucke, 2010), with converging evidence from various perspectives including theoretical (Mesulam, 1999), molecular (Spires-Jones and Hyman, 2014), animal model based (Bero *et al.,* 2011), and *in vivo* microdialysis and electrophysiological studies (Cirrito *et al.,* 2005). Three key facts regarding amyloid precursor protein (APP) processing are important to consider in this regard: processing of APP is influenced by (1) synaptic activity (Cirrito *et al.,* 2005) and plays an influential role in both (2) long-term potentiation, and (3) long-term depression (Palop and Mucke, 2010). From a signal-processing perspective within a system connected via synapses, these three factors ideally position APP processing to serve a 'gain' function (i.e., adjusting signal-to-noise properties depending on the context of the signals that are being passed along synapses over time). Viewed from this perspective, a natural link becomes apparent between system/ network wide signal processing in the brain and APP processing at the synapse. The

cascading network failure model of Alzheimer's disease (Jones *et al.,* 2016) postulates that large-scale compensatory shifts in brain connectivity, which initially appear as increased levels of functional connectivity, leads to network-wide changes in signal processing that have a large impact on APP processing and the likelihood of observing Aβ pathology in hubs of high connectivity.

It may be the case that local, within-network tau-associated disruptions trigger large-scale brain wide compensatory rearrangements which have been associated with amyloidosis in previous studies (Jones *et al.,* 2016). The observed plateauing of amyloidosis in this and other studies may mark a saturation of brain-wide compensatory changes for the original local network failure – with this original network containing only a subset of hubs. With an exhausted compensatory reserve, wide spread taurelated neurodegeneration proceeds within the inciting local network (Figure 1). This scenario, predicted by our model of a cascading network failure, would result in the characteristic spatiotemporal gaps observed for Aβ and tau. The observation that the relationship between network failure and τ-PET is partially, but not fully, mediate by Aβ-PET lends support to this model of network failure being causally related both to Aβ and tau (Figure 1 and 7). Our exploratory analyses supported the conclusion that there are two distinct patterns of posterior DMN connectivity associated with distinct tau-PET patterns as our model would predict (Figure 7D and 7E), with one pattern relating to Aβ (Figure 7B) and the other to NFQ (Figure 7C). Whilst alternate but currently unknown mechanisms may lead to the acceleration of molecular tau pathology by Aβ pathology, it seems likely that any such mechanism will need to include distributed brain network changes in order to incorporate all of the existing knowledge of Alzheimer's disease pathophysiology.

4.4 Limitations

The major limitation of this study is its cross-sectional nature, which has been a limitation in all previous studies of tau spatial patterns across the disease spectrum. That being said, we utilized several different methods of evaluating tau spatial patterns, each with unique biases, which yielded similar results regarding system-wide tau deposition. Moving forward, *in vivo* tau imaging will allow for longitudinal studies of tau spatial patterns to assess the sequential character of tau deposition. A potential important limitation of τ-PET is the off target binding to substrates unrelated to Alzheimer's disease tau pathology. However, our ICA-based analysis was able to isolate off-target signal (e.g., form the choroid plexus) and separate that from on-target signal in Braak staging regions. While it is still unclear what the pathologic correlates of age-associated marginally elevated levels of τ-PET signal in clinically normal subjects are, they do appear to be associated with worse cognition (Scholl *et al.,* 2016). Studies correlating *in vivo* τ-PET with histopathology in preclinical Alzheimer's disease are needed to better understand this phenomenon.

4.5 Conclusions

Our study is largely consistent with recent reports that the spatial distribution of τ-PET can appear both in 'Braak-like' and atypical distributions in an age associated manner involving functionally connected brain networks. However, it appears that τ-PET signal elevation within these systems may emerge throughout the affected network rather than sequentially,

as has been widely inferred from cross-sectional regional sampling of post-mortem tissue. In addition, we observed that tau is related to measures of network failure, and that this relationship is partially mediated by Aβ. This study strongly implicates large-scale brain networks in the pathophysiology of tau, offers support for a cascading network failure model of Alzheimer's disease, and encourages further testing of theories that incorporate large-scale network physiology into disease models linking tau and amyloid.

Supplementary Material

Refer to Web version on PubMed Central for supplementary material.

Acknowledgments

Abbreviations

Aβ	beta-amyloid
AD NI	Alzheimer's Disease Neuroimaging Initiative
APP	amyloid precursor protein
DMN	default mode network
FDG	flurodeoxyglucose
fMRI	functional MRI
IC	independent component
ICA	independent component analysis
NFQ	Network Failure Quotient
NFT	neurofibrillary tangles
ROI	region of interest
SNR	signal-to-noise ratio
SUVR	standardized uptake value ratio
τ-PET	[F-18]-AV-1451

References

Alafuzoff I, Arzberger T, Al-Sarraj S, Bodi I, Bogdanovic N, Braak H, Bugiani O, Del-Tredici K, Ferrer I, Gelpi E, Giaccone G, Graeber MB, Ince P, Kamphorst W, King A, Korkolopoulou P, Kovacs GG, Larionov S, Meyronet D, Monoranu C, Parchi P, Patsouris E, Roggendorf W, Seilhean D, Tagliavini F, Stadelmann C, Streichenberger N, Thal DR, Wharton SB, Kretzschmar H. Staging of neurofibrillary pathology in Alzheimer's disease: a study of the Brain Net Europe Consortium. Brain Pathol. 2008 Oct; 18(4):484–96. [PubMed: 18371174]

Albert MS, DeKosky ST, Dickson D, Dubois B, Feldman HH, Fox NC, Gamst A, Holtzman DM, Jagust WJ, Petersen RC, Snyder PJ, Carrillo MC, Thies B, Phelps CH. The diagnosis of mild cognitive impairment due to Alzheimer's disease: Recommendations from the National Institute on Aging-Alzheimer's Association workgroups on diagnostic guidelines for Alzheimer's disease. Alzheimers & Dementia. 2011 May; 7(3):270–9.

Alladi S, Xuereb J, Bak T, Nestor P, Knibb J, Patterson K, Hodges JR. Focal cortical presentations of Alzheimer's disease. Brain. 2007 Oct.130:2636–45. [PubMed: 17898010]

Baddeley, AD., Hitch, GJ. Working memory. In: Bower, GA., editor. The psychology of learning and motivation. New York: Academic Press; 1974. p. 47-89.

Bateman RJ, Xiong C, Benzinger TL, Fagan AM, Goate A, Fox NC, Marcus DS, Cairns NJ, Xie X, Blazey TM, Holtzman DM, Santacruz A, Buckles V, Oliver A, Moulder K, Aisen PS, Ghetti B, Klunk WE, McDade E, Martins RN, Masters CL, Mayeux R, Ringman JM, Rossor MN, Schofield PR, Sperling RA, Salloway S, Morris JC. Clinical and biomarker changes in dominantly inherited Alzheimer's disease. N Engl J Med. 2012 Aug 30; 367(9):795–804. [PubMed: 22784036]

Bates D, Machler M, Bolker BM, Walker SC. Fitting Linear Mixed-Effects Models Using lme4. J Stat Softw. 2015 Oct; 67(1):1–48.

Bennett DA, Schneider JA, Wilson RS, Bienias JL, Arnold SE. Neurofibrillary tangles mediate the association of amyloid load with clinical Alzheimer disease and level of cognitive function. Arch Neurol. 2004 Mar; 61(3):378–84. [PubMed: 15023815]

Bero AW, Yan P, Roh JH, Cirrito JR, Stewart FR, Raichle ME, Lee JM, Holtzman DM. Neuronal activity regulates the regional vulnerability to amyloid-beta deposition. Nat Neurosci. 2011 Jun. 14(6):750-U353. [PubMed: 21532579]

Braak H, Alafuzoff I, Arzberger T, Kretzschmar H, Del Tredici K. Staging of Alzheimer disease-associated neurofibrillary pathology using paraffin sections and immunocytochemistry. Acta neuropathologica. 2006 Oct; 112(4):389–404. [PubMed: 16906426]

Braak H, Braak E. Neuropathological stageing of Alzheimer-related changes. Acta neuropathologica. 1991; 82(4):239–59. [PubMed: 1759558]

Braak H, Braak E. Frequency of stages of Alzheimer-related lesions in different age categories. Neurobiol Aging. 1997 Jul-Aug;18(4):351–7. [PubMed: 9330961]

Braak H, Braak E, Bohl J, Reintjes R. Age, neurofibrillary changes, A beta-amyloid and the onset of Alzheimer's disease. Neurosci Lett. 1996 May 31; 210(2):87–90. [PubMed: 8783279]

Braak H, Thal DR, Ghebremedhin E, Del Tredici K. Stages of the pathologic process in Alzheimer disease: age categories from 1 to 100 years. J Neuropathol Exp Neurol. 2011 Nov; 70(11):960–9. [PubMed: 22002422]

Brier MR, Gordon B, Friedrichsen K, McCarthy J, Stern A, Christensen J, Owen C, Aldea P, Su Y, Hassenstab J, Cairns NJ, Holtzman DM, Fagan AM, Morris JC, Benzinger TL, Ances BM. Tau and Abeta imaging, CSF measures, and cognition in Alzheimer's disease. Sci Transl Med. 2016 May 11.8(338):338ra66.

Buckner RL, Sepulcre J, Talukdar T, Krienen FM, Liu H, Hedden T, Andrews-Hanna JR, Sperling RA, Johnson KA. Cortical hubs revealed by intrinsic functional connectivity: mapping, assessment of stability, and relation to Alzheimer's disease. The Journal of neuroscience : the official journal of the Society for Neuroscience. 2009 Feb 11; 29(6):1860–73. [PubMed: 19211893]

Calhoun VD, Adali T, Pearlson GD, Pekar JJ. A method for making group inferences from functional MRI data using independent component analysis. Hum Brain Mapp. 2001 Nov; 14(3):140–51. [PubMed: 11559959]

Cho H, Choi JY, Hwang MS, Kim YJ, Lee HM, Lee HS, Lee JH, Ryu YH, Lee MS, Lyoo CH. In vivo cortical spreading pattern of tau and amyloid in the Alzheimer's disease spectrum. Annals of Neurology. 2016 Jun 20.

Cirrito JR, Yamada KA, Finn MB, Sloviter RS, Bales KR, May PC, Schoepp DD, Paul SM, Mennerick S, Holtzman DM. Synaptic activity regulates interstitial fluid amyloid-beta levels in vivo. Neuron. 2005 Dec 22; 48(6):913–22. [PubMed: 16364896]

Crary JF, Trojanowski JQ, Schneider JA, Abisambra JF, Abner EL, Alafuzoff I, Arnold SE, Attems J, Beach TG, Bigio EH, Cairns NJ, Dickson DW, Gearing M, Grinberg LT, Hof PR, Hyman BT, Jellinger K, Jicha GA, Kovacs GG, Knopman DS, Kofler J, Kukull WA, Mackenzie IR, Masliah E, McKee A, Montine TJ, Murray ME, Neltner JH, Santa-Maria I, Seeley WW, Serrano-Pozo A, Shelanski ML, Stein T, Takao M, Thal DR, Toledo JB, Troncoso JC, Vonsattel JP, White CL 3rd, Wisniewski T, Woltjer RL, Yamada M, Nelson PT. Primary age-related tauopathy (PART): a common pathology associated with human aging. Acta neuropathologica. 2014 Dec; 128(6):755–66. [PubMed: 25348064]

Dickson DW, Crystal HA, Mattiace LA, Masur DM, Blau AD, Davies P, Yen SH, Aronson MK. Identification of normal and pathological aging in prospectively studied nondemented elderly humans. Neurobiology of aging. 1992 Jan-Feb;13(1):179–89. [PubMed: 1311804]

Duyckaerts C, Bennecib M, Grignon Y, Uchihara T, He Y, Piette F, Hauw JJ. Modeling the relation between neurofibrillary tangles and intellectual status. Neurobiol Aging. 1997 May-Jun;18(3):267–73. [PubMed: 9263190]

Greicius MD, Kimmel DL. Neuroimaging insights into network-based neurodegeneration. Curr Opin Neurol. 2012 Dec; 25(6):727–34. [PubMed: 23108250]

Gunter JL, Bernstein MA, Borowski BJ, Ward CP, Britson PJ, Felmlee JP, Schuff N, Weiner M, Jack CR. Measurement of MRI scanner performance with the ADNI phantom. Med Phys. 2009 Jun; 36(6):2193–205. [PubMed: 19610308]

Haberman RP, Koh MT, Gallagher M. Heightened cortical excitability in aged rodents with memory impairment. Neurobiology of aging. 2017 Jan 03.

Jack CR Jr, Bernstein MA, Fox NC, Thompson P, Alexander G, Harvey D, Borowski B, Britson PJ, J LW, Ward C, Dale AM, Felmlee JP, Gunter JL, Hill DL, Killiany R, Schuff N, Fox-Bosetti S, Lin C, Studholme C, DeCarli CS, Krueger G, Ward HA, Metzger GJ, Scott KT, Mallozzi R, Blezek D, Levy J, Debbins JP, Fleisher AS, Albert M, Green R, Bartzokis G, Glover G, Mugler J, Weiner MW. The Alzheimer's Disease Neuroimaging Initiative (ADNI): MRI methods. J Magn Reson Imaging. 2008 Apr; 27(4):685–91. [PubMed: 18302232]

Jack CR Jr, Knopman DS, Jagust WJ, Petersen RC, Weiner MW, Aisen PS, Shaw LM, Vemuri P, Wiste HJ, Weigand SD, Lesnick TG, Pankratz VS, Donohue MC, Trojanowski JQ. Tracking pathophysiological processes in Alzheimer's disease: an updated hypothetical model of dynamic biomarkers. Lancet Neurol. 2013 Feb; 12(2):207–16. [PubMed: 23332364]

Jack CR Jr, Knopman DS, Weigand SD, Wiste HJ, Vemuri P, Lowe V, Kantarci K, Gunter JL, Senjem ML, Ivnik RJ, Roberts RO, Rocca WA, Boeve BF, Petersen RC. An operational approach to National Institute on Aging-Alzheimer's Association criteria for preclinical Alzheimer disease. Ann Neurol. 2012 Jun; 71(6):765–75. [PubMed: 22488240]

Jack CR Jr, Wiste HJ, Lesnick TG, Weigand SD, Knopman DS, Vemuri P, Pankratz VS, Senjem ML, Gunter JL, Mielke MM, Lowe VJ, Boeve BF, Petersen RC. Brain beta-amyloid load approaches a plateau. Neurology. 2013 Mar 5; 80(10):890–6. [PubMed: 23446680]

Jack CR Jr, Wiste HJ, Weigand SD, Therneau TM, Lowe VJ, Knopman DS, Gunter JL, Senjem ML, Jones DT, Kantarci K, Machulda MM, Mielke MM, Roberts RO, Vemuri P, Reyes DA, Petersen RC. Defining imaging biomarker cut points for brain aging and Alzheimer's disease. Alzheimers Dement. 2017 Mar; 13(3):205–16. [PubMed: 27697430]

Johnson KA, Schultz A, Betensky RA, Becker JA, Sepulcre J, Rentz D, Mormino E, Chhatwal J, Amariglio R, Papp K, Marshall G, Albers M, Mauro S, Pepin L, Alverio J, Judge K, Philiossaint M, Shoup T, Yokell D, Dickerson B, Gomez-Isla T, Hyman B, Vasdev N, Sperling R. Tau positron emission tomographic imaging in aging and early Alzheimer disease. Ann Neurol. 2016 Jan; 79(1):110–9. [PubMed: 26505746]

Jones DT, Knopman DS, Gunter JL, Graff-Radford J, Vemuri P, Boeve BF, Petersen RC, Weiner MW, Jack CR Jr. Cascading network failure across the Alzheimer's disease spectrum. Brain : a journal of neurology. 2016 Feb; 139(Pt 2):547–62. [PubMed: 26586695]

Jones DT, Vemuri P, Murphy MC, Gunter JL, Senjem ML, Machulda MM, Przybelski SA, Gregg BE, Kantarci K, Knopman DS, Boeve BF, Petersen RC, Jack CR Jr. Non-stationarity in the "resting brain's" modular architecture. PLoS One. 2012; 7(6):e39731. [PubMed: 22761880]

Klunk WE, Engler H, Nordberg A, Wang Y, Blomqvist G, Holt DP, Bergstrom M, Savitcheva I, Huang GF, Estrada S, Ausen B, Debnath ML, Barletta J, Price JC, Sandell J, Lopresti BJ, Wall A, Koivisto P, Antoni G, Mathis CA, Langstrom B. Imaging brain amyloid in Alzheimer's disease with Pittsburgh Compound-B. Annals of Neurology. 2004; 55(3):306–19. [PubMed: 14991808]

Lowe VJ, Curran G, Fang P, Liesinger AM, Josephs KA, Parisi JE, Kantarci K, Boeve BF, Pandey MK, Bruinsma T, Knopman DS, Jones DT, Petrucelli L, Cook CN, Graff-Radford NR, Dickson DW, Petersen RC, Jack CR Jr, Murray ME. An autoradiographic evaluation of AV-1451 Tau PET in dementia. Acta Neuropathol Commun. 2016; 4(1):58. [PubMed: 27296779]

Maass A, Landau S, Baker SL, Horng A, Lockhart SN, La Joie R, Rabinovici GD, Jagust WJ. Comparison of multiple tau-PET measures as biomarkers in aging and Alzheimer's disease. Neuroimage. 2017 Aug 15.157:448–63. [PubMed: 28587897]

McKhann GM, Knopman DS, Chertkow H, Hyman BT, Jack CR, Kawas CH, Klunk WE, Koroshetz WJ, Manly JJ, Mayeux R, Mohs RC, Morris JC, Rossor MN, Scheltens P, Carrillo MC, Thies B, Weintraub S, Phelps CH. The diagnosis of dementia due to Alzheimer's disease: Recommendations from the National Institute on Aging-Alzheimer's Association workgroups on diagnostic guidelines for Alzheimer's disease. Alzheimers & Dementia. 2011 May; 7(3):263–9.

Mesulam MM, Weintraub S, Rogalski EJ, Wieneke C, Geula C, Bigio EH. Asymmetry and heterogeneity of Alzheimer's and frontotemporal pathology in primary progressive aphasia. Brain. 2014 Apr.137:1176–92. [PubMed: 24574501]

Mesulam NM. Neuroplasticity failure in Alzheimer's disease: Bridging the gap between plaques and tangles. Neuron. 1999 Nov; 24(3):521–9. [PubMed: 10595506]

Mishra S, Gordon BA, Su Y, Christensen J, Friedrichsen K, Jackson K, Hornbeck R, Balota DA, Cairns NJ, Morris JC, Ances BM, Benzinger TLS. AV-1451 PET imaging of tau pathology in preclinical Alzheimer disease: Defining a summary measure. Neuroimage. 2017 [2017/07/26/]

Murray ME, Graff-Radford NR, Ross OA, Petersen RC, Duara R, Dickson DW. Neuropathologically defined subtypes of Alzheimer's disease with distinct clinical characteristics: a retrospective study. Lancet Neurology. 2011 Sep; 10(9):785–96. [PubMed: 21802369]

Ossenkoppele R, Schonhaut DR, Scholl M, Lockhart SN, Ayakta N, Baker SL, O'Neil JP, Janabi M, Lazaris A, Cantwell A, Vogel J, Santos M, Miller ZA, Bettcher BM, Vossel KA, Kramer JH, Gorno-Tempini ML, Miller BL, Jagust WJ, Rabinovici GD. Tau PET patterns mirror clinical and neuroanatomical variability in Alzheimer's disease. Brain. 2016 Mar 8.

Palop JJ, Mucke L. Amyloid-beta-induced neuronal dysfunction in Alzheimer's disease: from synapses toward neural networks. Nat Neurosci. 2010 Jul; 13(7):812–8. [PubMed: 20581818]

Petersen, RC., editor. Mild cognitive impairment: Aging to Alzheimer's disease. New York, NY, US: Oxford University Press; 2003.

Petersen RC. Mild cognitive impairment as a diagnostic entity. J Intern Med. 2004 Sep; 256(3):183–94. [PubMed: 15324362]

Petersen, RC., Graff-Radford, J. Bradley's neurology in clinical practice / [edited by] Robert B. Daroff … [et al.]. In: Daroff, RB.Jankovic, J.Mazziotta, JC., Pomeroy, SL., editors. Bradley's neurology in clinical practice. 7. Philadelphia, PA: Elsevier/Saunders; 2016. p. 1380-421.

Raj A, Kuceyeski A, Weiner M. A network diffusion model of disease progression in dementia. Neuron. 2012 Mar 22; 73(6):1204–15. [PubMed: 22445347]

Roberts RO, Geda YE, Knopman DS, Cha RH, Pankratz VS, Boeve BF, Ivnik RJ, Tangalos EG, Petersen RC, Rocca WA. The Mayo Clinic Study of Aging: design and sampling, participation, baseline measures and sample characteristics. Neuroepidemiology. 2008; 30(1):58–69. [PubMed: 18259084]

Saper CB, Wainer BH, German DC. Axonal and transneuronal transport in the transmission of neurological disease: potential role in system degenerations, including Alzheimer's disease. Neuroscience. 1987 Nov; 23(2):389–98. [PubMed: 2449630]

Scholl M, Lockhart SN, Schonhaut DR, O'Neil JP, Janabi M, Ossenkoppele R, Baker SL, Vogel JW, Faria J, Schwimmer HD, Rabinovici GD, Jagust WJ. PET Imaging of Tau Deposition in the Aging Human Brain. Neuron. 2016 Mar 2; 89(5):971–82. [PubMed: 26938442]

Schwarz AJ, Yu P, Miller BB, Shcherbinin S, Dickson J, Navitsky M, Joshi AD, Devous MD Sr, Mintun MS. Regional profiles of the candidate tau PET ligand 18F-AV-1451 recapitulate key features of Braak histopathological stages. Brain. 2016 Mar 2.

Seeley WW, Crawford RK, Zhou J, Miller BL, Greicius MD. Neurodegenerative diseases target large-scale human brain networks. Neuron. 2009 Apr 16; 62(1):42–52. [PubMed: 19376066]

Senjem ML, Gunter JL, Shiung MM, Petersen RC, Jack CR Jr. Comparison of different methodological implementations of voxel-based morphometry in neurodegenerative disease. Neuroimage. 2005 Jun; 26(2):600–8. [PubMed: 15907317]

Sepulcre J, Schultz AP, Sabuncu M, Gomez-Isla T, Chhatwal J, Becker A, Sperling R, Johnson KA. In Vivo Tau, Amyloid, and Gray Matter Profiles in the Aging Brain. J Neurosci. 2016 Jul 13; 36(28): 7364–74. [PubMed: 27413148]

Spires-Jones TL, Hyman BT. The Intersection of Amyloid Beta and Tau at Synapses in Alzheimer's Disease. Neuron. 2014 May 21; 82(4):756–71. [PubMed: 24853936]

Stam CJ. Modern network science of neurological disorders. Nat Rev Neurosci. 2014 Oct; 15(10):683–95. [PubMed: 25186238]

Tingley D, Yamamoto T, Hirose K, Keele L, Imai K. mediation: R Package for Causal Mediation Analysis. J Stat Softw. 2014 Aug.59(5)

Vemuri P, Senjem ML, Gunter JL, Lundt ES, Tosakulwong N, Weigand SD, Borowski BJ, Bernstein MA, Zuk SM, Lowe VJ, Knopman DS, Petersen RC, Fox NC, Thompson PM, Weiner MW, Jack CR Jr, Alzheimer's Disease Neuroimaging I. Accelerated vs. unaccelerated serial MRI based TBM-SyN measurements for clinical trials in Alzheimer's disease. Neuroimage. 2015 Jun.113:61–9. [PubMed: 25797830]

Villemagne VL, Burnham S, Bourgeat P, Brown B, Ellis KA, Salvado O, Szoeke C, Macaulay SL, Martins R, Maruff P, Ames D, Rowe CC, Masters CL. Amyloid beta deposition, neurodegeneration, and cognitive decline in sporadic Alzheimer's disease: a prospective cohort study. The Lancet Neurology. 2013 Apr; 12(4):357–67. [PubMed: 23477989]

Walsh DM, Selkoe DJ. A critical appraisal of the pathogenic protein spread hypothesis of neurodegeneration. Nat Rev Neurosci. 2016 Mar 18; 17(4):251–60. [PubMed: 26988744]

Warren JD, Fletcher PD, Golden HL. The paradox of syndromic diversity in Alzheimer disease. Nat Rev Neurol. 2012 Aug; 8(8):451–64. [PubMed: 22801974]

Warren JD, Rohrer JD, Schott JM, Fox NC, Hardy J, Rossor MN. Molecular nexopathies: a new paradigm of neurodegenerative disease. Trends Neurosci. 2013 Oct; 36(10):561–9. [PubMed: 23876425]

Whitwell JL, Jones DT, Duffy JR, Strand EA, Machulda MM, Przybelski SA, Vemuri P, Gregg BE, Gunter JL, Senjem ML, Petersen RC, Jack J CR, Josephs KA. Working memory and language network dysfunction in logopenic aphasia: a task-free fMRI comparison to Alzheimer's dementia. Neurobiology of aging. 2015 in press.

Wiepert D, Lowe V, Knopman D, Boeve B, Graff-Radford J, Petersen R, Jack C Jr, Jones D. A Robust Biomarker of Large-Scale Network Failure in Alzheimer's Disease. Alzheimer's and Dementia: Diagnosis, Assessment & Disease Monitoring. 2017; 6:152–61.

Wood, SN. Generalized additive models : an introduction with R. Boca Raton: Chapman & Hall/CRC; 2006.

Xia CF, Arteaga J, Chen G, Gangadharmath U, Gomez LF, Kasi D, Lam C, Liang Q, Liu C, Mocharla VP, Mu F, Sinha A, Su H, Szardenings AK, Walsh JC, Wang E, Yu C, Zhang W, Zhao T, Kolb HC. [(18)F]T807, a novel tau positron emission tomography imaging agent for Alzheimer's disease. Alzheimers Dement. 2013 Nov; 9(6):666–76. [PubMed: 23411393]

Zhou J, Gennatas ED, Kramer JH, Miller BL, Seeley WW. Predicting regional neurodegeneration from the healthy brain functional connectome. Neuron. 2012 Mar 22; 73(6):1216–27. [PubMed: 22445348]
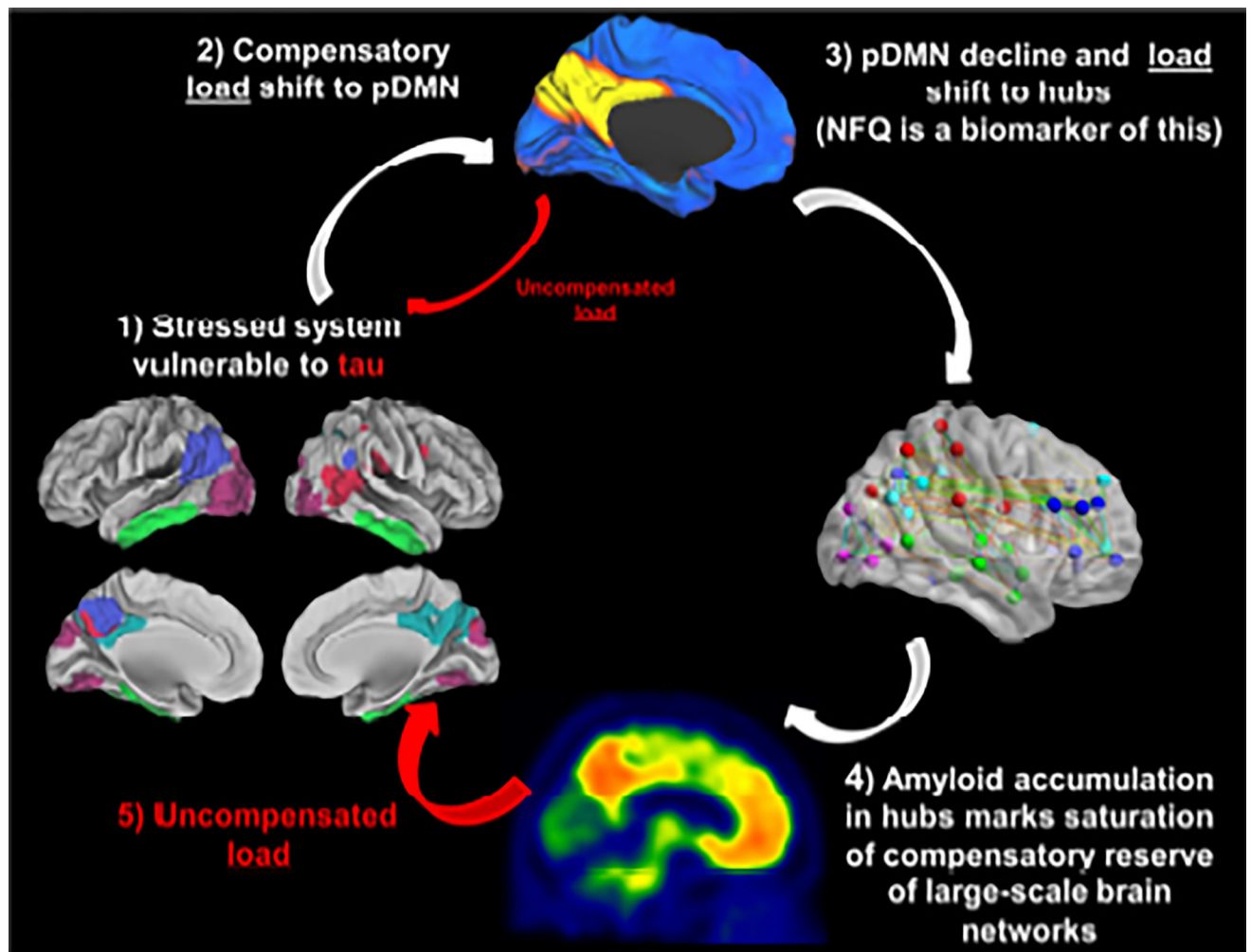
Figure 1. Cascading Network Failure, Amyloid, and Tau

This figure is a schematic of the hypothetical model relating large-scale brain networks, beta-amyloid, and tau across the Alzheimer's disease spectrum and serves as an outline of the current study. 1) A brain surface rendering with 5 key regions of spatially independent tau deposition patterns (see Figures 2 and 3). In this schematic, these regions mark the potential combinations of brain regions that support functional brain networks that may experience high information processing load, or stress, which may predispose to a tau-related degenerative process. 2) In order to avert system failure and hence clinical impairment, the brain regions involved in these functional networks may shift their processing load to the posterior DMN which serves as the core processing hub in the brain (represented by the blue and yellow brain rendering). Any uncompensated load may lead to early low levels of tau accumulation in the stressed system during the preclinical disease phase and is represented by the small red arrow in the schematic. Whether this process occurs focally and sequentially throughout connected brain regions, or emerges simultaneously across the system, as this model may predict, is explored in another set of analyses (Figures 4–6). 3) The posterior DMN becomes overloaded and begins to shift its processing load to other connectivity hubs (represented by the ball-and-stick brain

rendering). This posterior DMN decline, accompanied by increased connectivity between the posterior DMN and other brain systems, is quantified in the recently developed biomarker termed the Network Failure Quotient (NFQ), see (Wiepert et al., 2017) for details. 4) This increased load leads to noisier synaptic activity, and alterations in APP processing occur in an effort to compensate. The altered APP processing eventually leads to amyloid plaque formation (represented by a single subject's amyloid PET scan at the bottom of the figure) and a saturation of synaptic compensation, and therefore functional compensation. 5) With an inability to shift additional processing load, the uncompensated stress in the original system now leads to a rapid acceleration of the previously indolent tau-associated neurodegenerative process (large red arrow). This proposed relationship between NFQ, beta-amyloid and tau are explored in a mediation analyses (Figure 7).
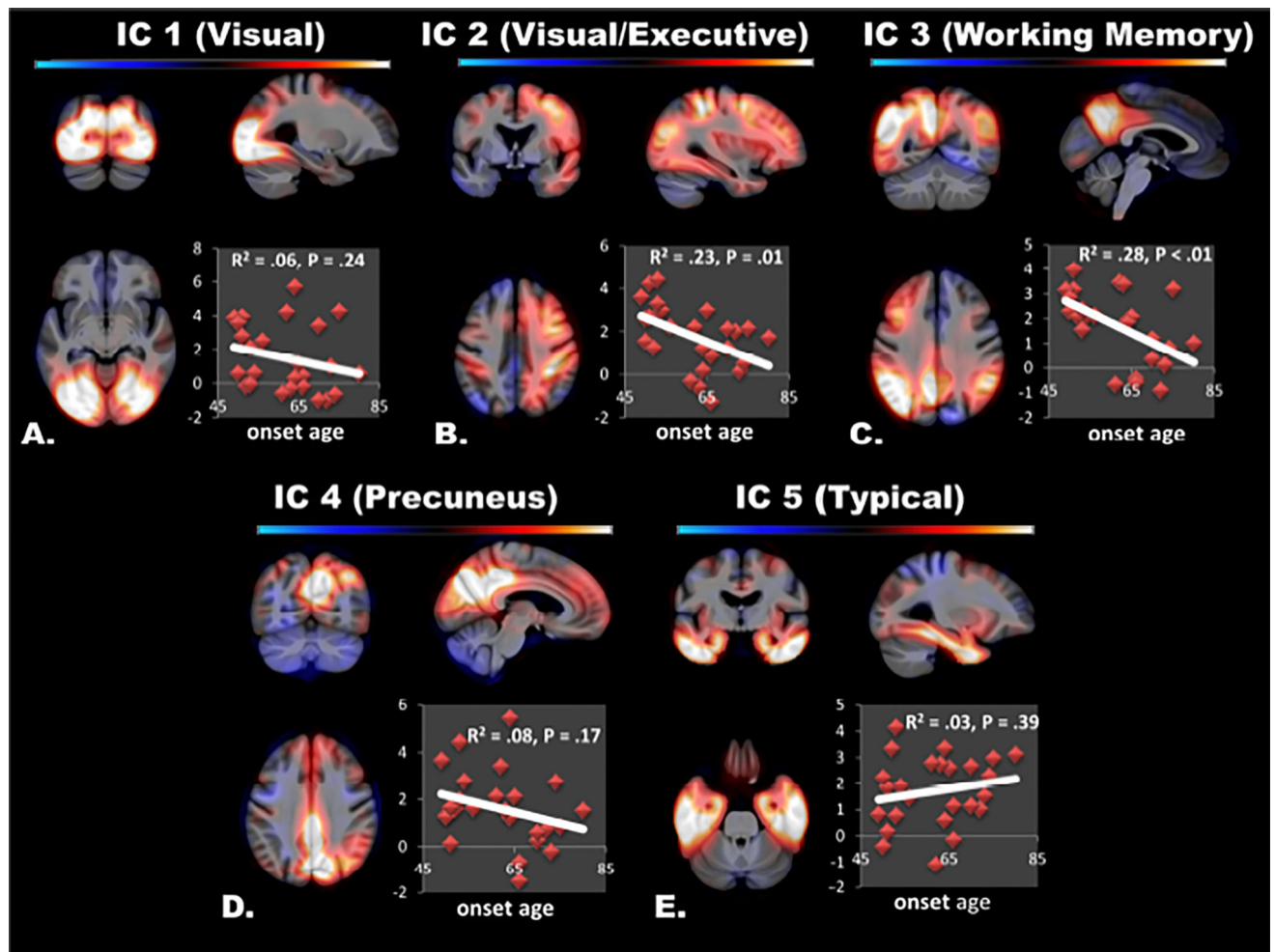
Figure 2. Spatial Patterns of Tau Deposition

The spatial extent of the five biologically relevant τ-PET independent components are overlaid on orthogonal slices of a template brain (color bar encodes z-score from −5 to 5). Inset, the subject component scores are plotted vs. age-of-onset for the dementia cases. Note that there are trends towards higher loadings in younger onset subjects in atypical 'non-Braak-like' patterns (A–D), but not in the typical 'Braak-like' pattern (E).
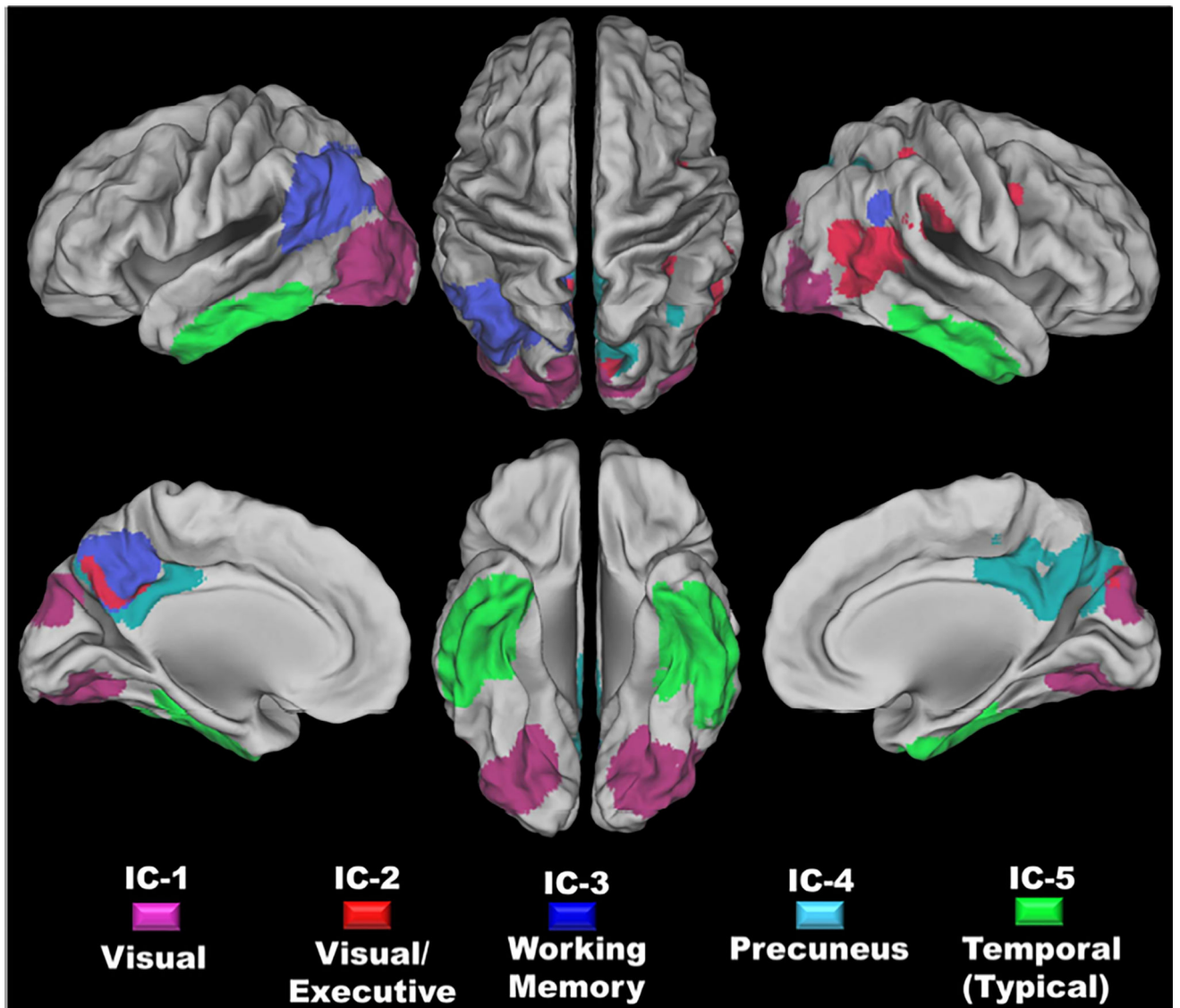
Figure 3. Regions of Interest derived from the Five Tau Deposition Patterns
Each of the five tau deposition patterns was used to derive a ROI by binarizing the IC maps
using a hard threshold of a z-score of five. The spatial extents of these ROIs are overlaid on
a surface rendering in this figure, with each IC color coded (see the legend at the bottom of
the figure). The orange areas in the figure demarcate regions of overlap between two ROIs.
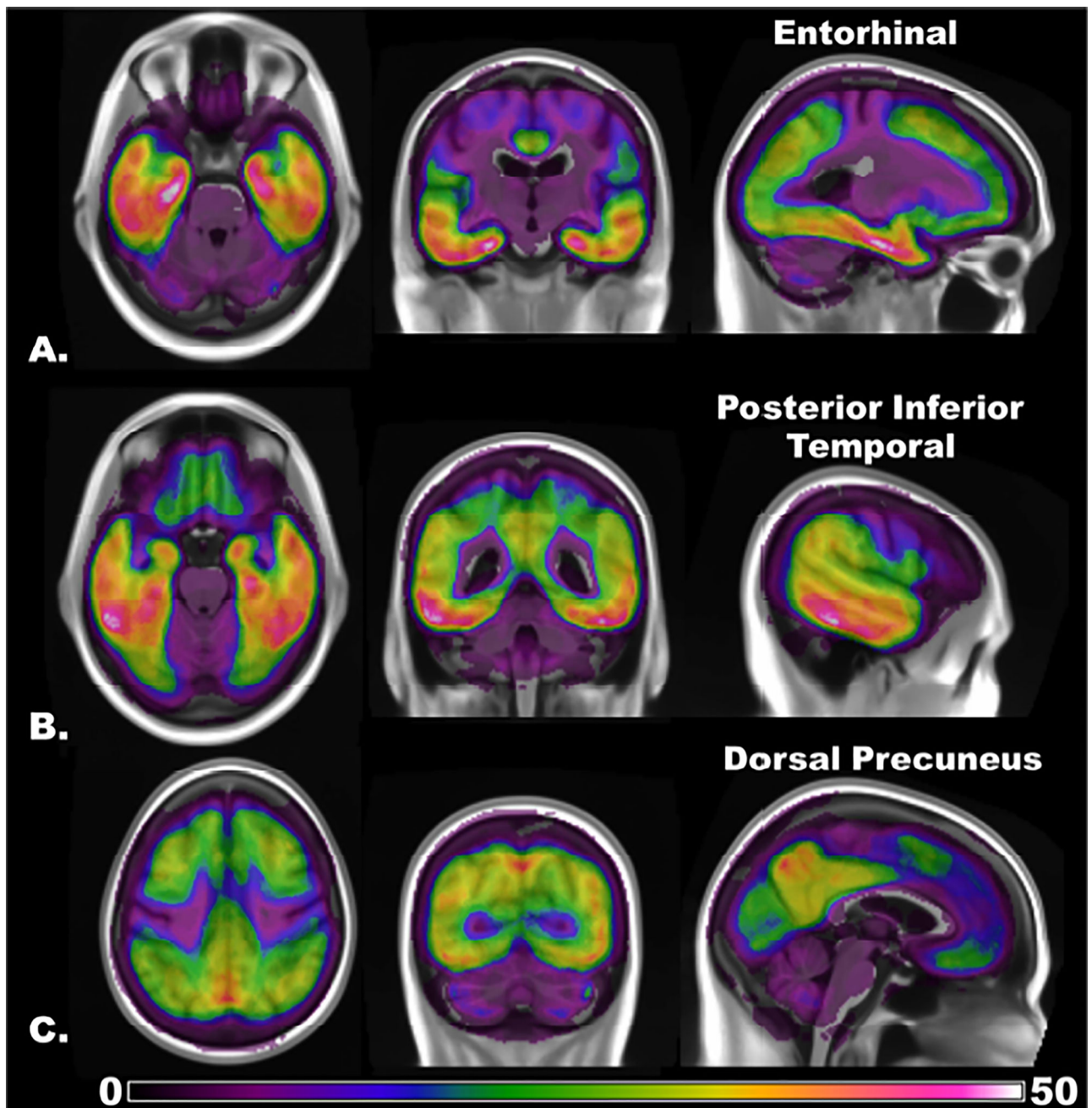
Figure 4. Voxel-Wise Frequency Map of Elevated τ-PET Signal across the Alzheimer's Spectrum
The frequency with which a voxel has abnormally elevated τ-PET signal (z-score greater than 3) across the entire sample, excluding the subjects used to anchor the threshold (n = 168), is color coded from least (zero subjects) to maximum (53 subjects). The same frequency map is overlaid on orthogonal slices chosen to highlight peak regions in the A) entorhinal, B) posterior inferior temporal, and the C) dorsal precuneus. Lowering the threshold to determine positivity increases the frequency count, but the spatial pattern of abnormal regions does not change (see the main text for details).
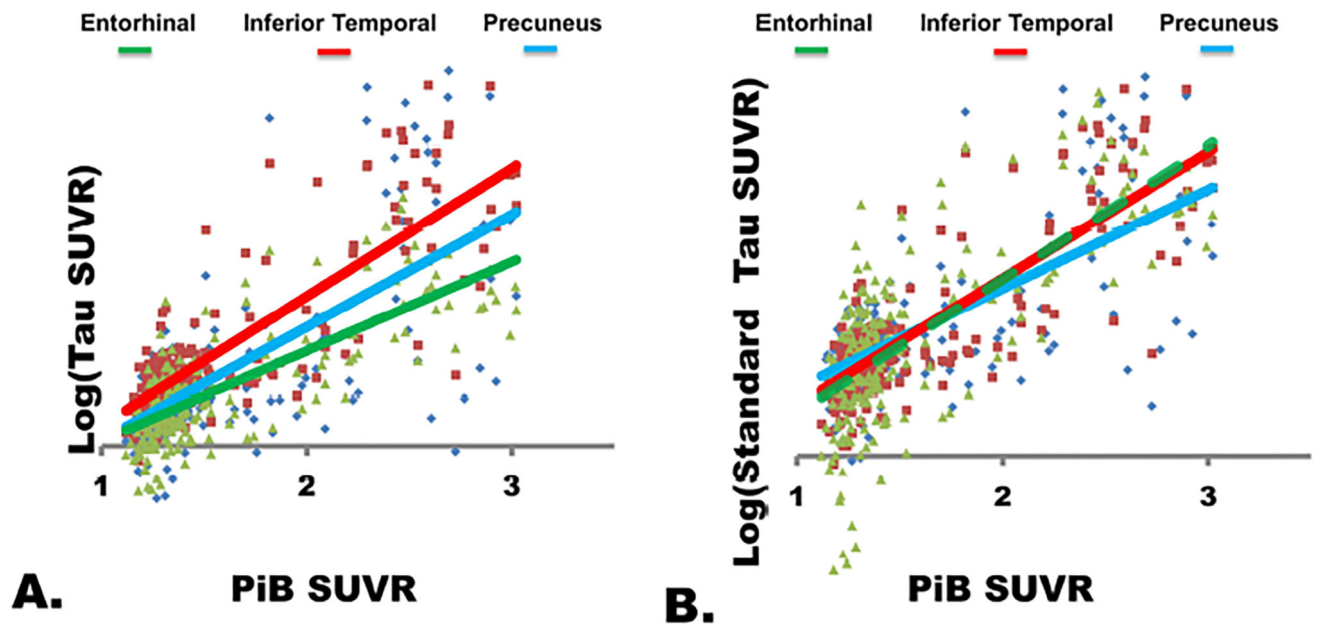
Figure 5. Brain Region Effect on the relationship between τ-PET and Aβ-PET
A) The log transformed τ-PET signal from each of three brain regions (entorhinal [green], inferior temporal [red], and dorsal precuneus [cyan] from Figure 4) is plotted vs Aβ-PET SUVR. Surprisingly, the entorhinal cortex shows the lowest magnitude increase and does not have a steeper slope than the other brain regions. B) However, once the values in each region are standardized with respect to the biological signal-to-noise properties in each region, there is no difference between the entorhinal and inferior temporal brain regions, but the precuneus has a smaller slope than both of these regions.
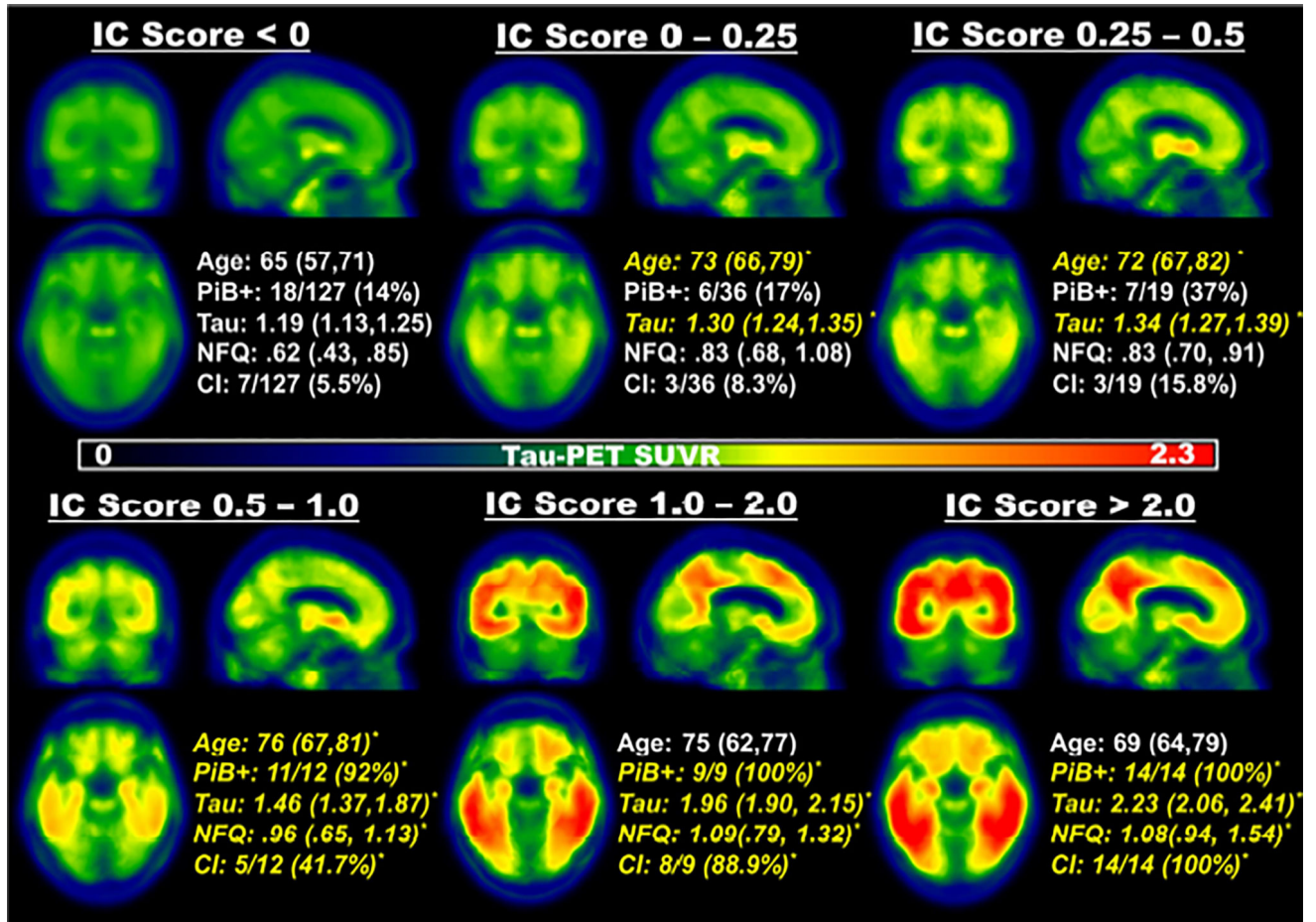
Figure 6. The Emergence of System-Wide Tau Signal, Amyloidosis, Network Failure, and Cognitive Impairment with Advancing Subject Component Score

The τ-PET scans were averaged within subjects grouped by the Braak-like independent component (IC 5) z-scores. The groupings are illustrated with colored boxes in Supplementary Figure 2. These average values are displayed in orthogonal slices, with the color-bar encoding the median τ-PET SUVR, highlighting the emergence of elevated signal throughout brain regions rather than step-wise as might be expected. Inset, are average variables (median and 1st and 3rd quartiles for age, τ-PET SUVR within the IC 5 ROI, and network failure quotient) and counts (number of subjects with Aβ-PET SUVR greater than 1.5 and number of subjects that are clinically impaired [either mild cognitive impairment or dementia]). Variables that are significantly different relative to the first IC group (IC score < 0) are italicized in yellow font and marked with an asterisk. Kruskal-Wallis one-way ANOVA was used for continuous variables, with post hoc Mann-Whitney U-tests for pair-wise differences. Chi-squared tests were used for categorical variables.
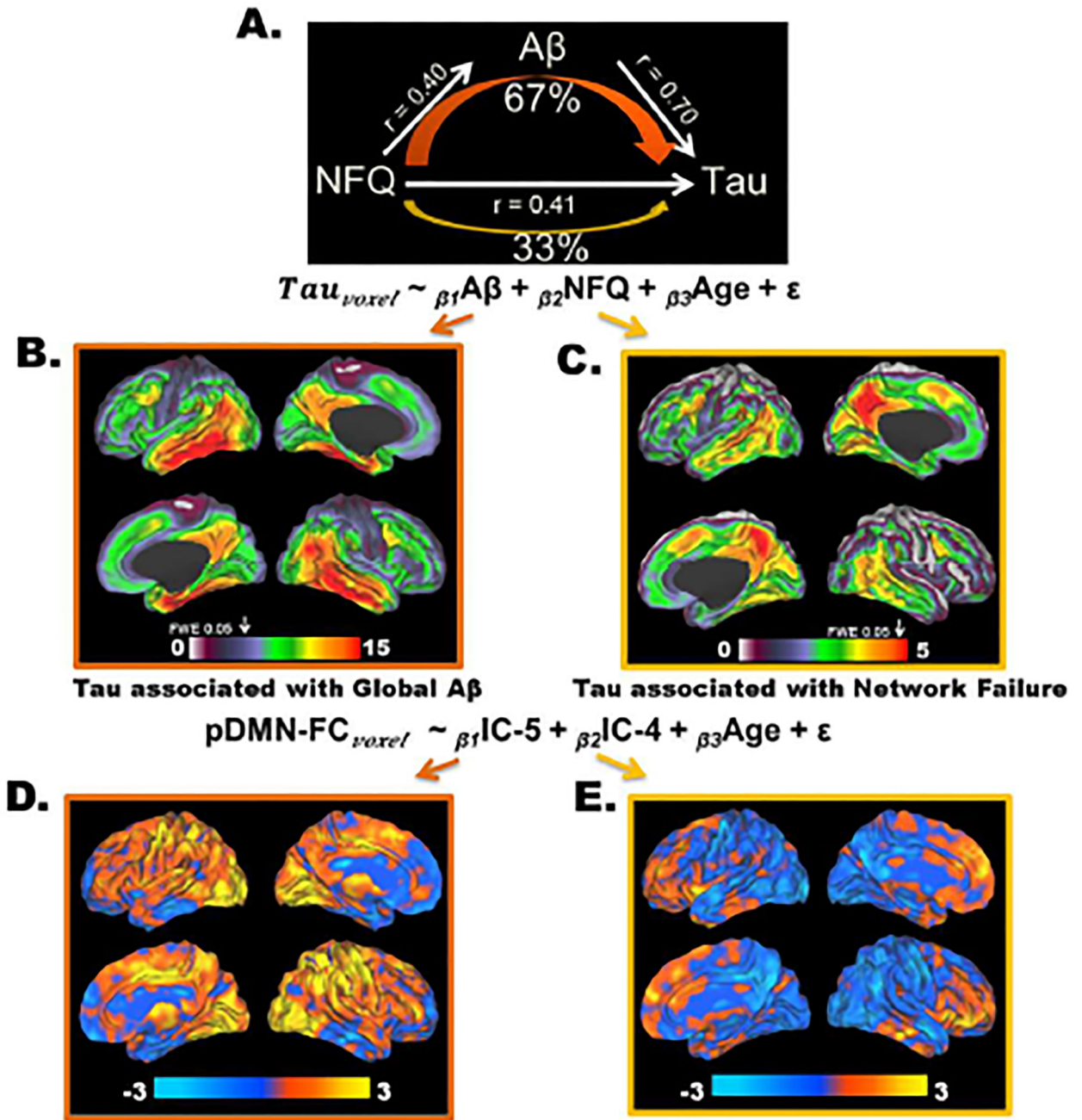
Figure 7. Amyloid Partially Mediates the Relationship between Network Failure and Tau
A) A schematic of the mediation analyses, across all subjects (n = 218), testing predictions
made by the cascading network failure model of Alzheimer's disease, that the majority of
the association between network failure (NFQ) and tau would be mediated by the amyloid
phase of the disease process. This schematic shows that NFQ is related both to Aβ and tau,
but ~67% of the association between NFQ and tau is mediated by Aβ. The spatial pattern of
these effects is investigated voxel-wise within the linear model expressed at the bottom of
the mediation analyses schematic. B) A map of the t-score (ranging from 0 to 15) for the Aβ
term in the model at each voxel is displayed on a surface rendering. C) A map of the t-score

(ranging from 0 to 5) for the NFQ term in the model at each voxel is displayed on a surface rendering. The voxel-wise FWE rate of 0.05 is indicated by the white arrow above each color bar in B and C. D) A map of the t-score (ranging from −3 to 3) for the IC-5 term in the model predicting posterior DMN functional connectivity at each voxel is displayed on a surface rendering. E) A map of the t-score (ranging from −3 to 3) for the IC-4 term in the model predicting posterior DMN functional connectivity at each voxel is displayed on a surface rendering. None of the results in D and E were greater that the voxel-wise FWE significance level.

Table 1

Patient Characteristics

Characteristic	All (n=218)	Clinically Normal (n=177)	Impaired (n=41)
Age, years			
Median (IQR)	68 (59,74)	67 (58,73)	68(63,75)
Min, Max	31,90	31,90	55,83
Male gender, no. (%)	126 (58%)	102 (58%)	24 (59%)
Education, years			
Median (IQR)	16 (13,18)	16 (14,17)	16 (13,18)
Min, Max	12,20	12,20	12,20
MMSE			
Median (IQR)	29 (28,29)	29 (28,29)	22 (17,26)
Min, Max	6,30	23,30	6,30
PIB PET, SUVR			
Median (IQR)	1.35 (1.27,1.69)	1.32 (1.26,1.40)	2.47 (2.15,2.69)
Min, Max	1.12,3.02	1.12,2.73	1.51,3.02
>1.4, no. (%)	89 (41%)	48 (27%)	41 (100%)
>1.5, no. (%)	66 (30%)	25 (14%)	41 (100%)